Research Article Vol. 24, No. 23 | 14 Nov 2016 | OPTICS EXPRESS 26646

Optics EXPRESS

# Divergent groove gratings: wavelength scanning in fixed geometry spectrometers

MICHAEL C. HETTRICK *

*Hettrick Scientific, Fuchu-shi Tokyo, Japan 183-0002*

**hettrickscientific@gmail.com*

**Abstract**: A new geometric scheme translates a diffraction grating along the straight central groove of an exponentially curved pattern. Lit by a stationary incident beam, the two-dimensional pattern scales isotropically, scanning wavelength without change to any angles, macroscopic distances, curvatures or aberrations. This is exemplified by a new class of self-focused grating monochromator, analyzed by rigorous light-path expansion and numerical raytracing. All spectral aberrations in pure meridional powers (including defocus, coma and spherical aberration) cancel for any angular deviation, magnification and translation range. The residual mixed powers yield $\Delta\lambda/\lambda = 10^{-3} \sim 10^{-5}$ in the soft x-ray for plane and concave gratings at grazing incidence. Over the visible spectrum, $\Delta\lambda/\lambda \sim 10^{-4}$ is shown for plane gratings mounted at Littrow and at normal incidence in reflection or transmission.



**OCIS codes:** (220.2740) Geometrical optical design; (050.1950) Diffraction gratings; (120.4140) Monochromators; (080.1005) Aberration expansions; (340.7480) Soft x-rays.

## References and links

1. M.C. Hettrick, "A Single-Element Plane Grating Monochromator," Photonics **3(1)**, 3, 1-44 (2016).
2. D.E. Aspnes, "High-efficiency concave-grating monochromator with wavelength-independent focusing characteristics," J. Opt. Soc. Am. **72**, 1056-1061 (1982).
3. E. Ishiguro, M. Suzui, J. Yamazaki, E. Nakamura, K. Sakai, O. Matsudo, N. Mizutani, K. Fukui and M. Watanabe, " Constant deviation monochromator for the range 100 A $\leq \lambda \leq$ 1000 A," Rev. Sci. Instrum. **60**, 2105-2108 (1989).
4. M.C. Hettrick, "In-focus monochromator: theory and experiment of a new grazing incidence mounting," Appl. Opt. **29**, 4531- 4535 (1990).
5. A. April and N. McCarthy, "Control of spectral aberrations in a monochromator using a plane holographic chirped grating," Appl. Opt. **47**, 2750-2759 (2008).
6. A.N. Simonov, S. Grabarnik and G. Vdovin, "Stretchable diffraction gratings for spectrometry," Opt. Express **15**, 9784-9792 (2007).
7. T. Glaser, S. Schröter, S. Fehling, R. Pöhlmann and M. Vlček, "Nanostructuring of organic and chalcogenide resists by direct DUV laser beam writing," Electron. Lett. **40**, 176-177 (2004).
8. D. Radtke and U. Zeitner, "Laser-lithography on non-planar surfaces," Opt. Express **16**, 1167-1174 (2007).
9. E.W. Palmer, M.C. Hutley, A. Franks, J.F. Verrill and B. Gale, "Diffraction gratings," Rep. Prog. Phys. **38**, 975-1048 (1975).
10. T. Harada, S. Moriyama, T. Kita and Y. Kondo, "Development of numerical control ruling engine for stigmatic concave grating," J. Jpn. Soc. Precision Eng. **42**, 888-892 (1976).
11. F. Polack, B. Lagarde, M. Idir, A.L. Cloup and E. Jourdain,"Variable groove depth gratings and their applications in soft x-ray monochromators,"Am. Inst. Phys., Conf. Proc. **879**, 639-643 (2007).
12. M.C. Hettrick, "Corrections to 'A Single-Element Plane Grating Monochromator'," http://www.hettrickscientific.com (2016).
13. M. Lampton, "BEAM FOUR: Optical ray tracer, v. 194," http://www.stellarsoftware.com (priv. comm., 2016).
14. H.A. Rowland, "On concave gratings for optical purposes," Phil. Mag. **16**, 197-210 (1883).

## 1. Introduction

The author has recently presented a class of single-element high-resolution plane grating monochromator having fixed principal ray directions, object distance and image distance [1]. That solution correlates multiple-axis grating rotations to correct the geometrical aberrations over a broad range in scanned wavelength. As an alternative, the present work employs only translation of the grating along its surface, absent any rotations or multiple motions.

#276424 http://dx.doi.org/10.1364/OE.24.026646
Journal © 2016 Received 22 Sep 2016; revised 27 Oct 2016; accepted 28 Oct 2016; published 9 Nov 2016

Optics EXPRESS

Previous geometries employing grating translation are few and limited to motions within a meridional plane normal to parallel grooves. Aspnes [2] proposed a sagittally curved cylindrical grating translating along its axis of symmetry and having an exponential variation in the groove spacings. This is the only fixed geometry design to date, and would exhibit both stigmatism and spectral resolution independent of the scan wavelength. However, the grating manufacture is challenging for use at grazing angles: a) the exponential spacing does not conform to patterns from interference lithography, thus is difficult to provide on the steeply curved surface, and b) spectral focusing to first and second powers determines the translation, requiring the grating ruled width significantly exceed its illuminated portion. Also, cylindrical symmetry constrains the magnification to be $\sin^2\alpha/\sin^2\beta$ (where $\alpha$ and $\beta$ are the graze angles of incidence and diffraction), which is undesirably far from unity and leaves insufficient freedom to eliminate third-power "spherical aberration". Nonetheless, Aspnes' insight offers maximum image brightness for a monochromator with moderate-high spectral resolution. Ishiguro et. al. [3] employed a large magnitude translation of a grazing incidence concave grating - plane mirror system. This corrects for first-power defocusing as the grating rotates about its pole to scan wavelength, while preserving the (parallel) optical axes entering and exiting the optics pair. Hettrick [4] eliminated the first and second power spectral aberrations by small translation of a varied line-space concave grating along its tangent plane. To scan wavelength, this motion was combined with rotation about an axis fixed in space. April and McCarthy [5] translated a near-normal-incidence plane grating (recorded by two-beam interference) in a direction which numerically minimized the net spectral aberration to third power. This trajectory, almost normal to the surface, changed both the object and image distances while the wavelength was scanned due to the varying angle of diffraction.

In the above four geometries, the critical tasks of scanning wavelength and controlling aberrations depend on the same optical parameters (e.g. the angles of incidence and diffraction, the varied spacing and the translation) specified in the meridional direction. This over-constrains the parameters and limits the spectral resolution. In the present work, these tasks are executed in orthogonal directions, an approach which is anticipated to improve performance and enable a practical design using existing technologies of grating manufacture.

## 2. Basic scheme

Consider an optical system employing a diffraction grating, wherein each of the macroscopic operational elements are fixed in position, angular orientation and curvature. The only variable in such an otherwise static geometry is the scale of the diffracting structure on the illuminated portion of the grating. In effect, the groove pattern may only uniformly expand or contract, to increase or decrease the scaled wavelength which is diffracted to a given image position. The technology to do this directly (by literally stretching an elastomeric grating [6] or constructing dynamically programmable meta-surfaces) at diffraction-limited accuracy is unlikely to be available soon, particularly for use at short wavelengths. However, a current practical means of effectively producing this result, albeit with residual aberrations, is illustrated in Fig. 1. Physically static grooves curve away from the line along which the grating translates, thereby placing a continuously-scaled groove pattern in the path of a stationary incident beam. This scheme provides the following inherent attributes: 1) the mechanical stability, accuracy and simplicity of rectilinear translation, 2) a fractional spectral resolution ($\Delta\lambda/\lambda$) which is independent of the wavelength, 3) a fixed principal ray (in-and-out) and 4) fixed angular apertures (in-and-out).

Except when giving numerical examples, dimensionless quantities (in *italic font*) will typically be used, normalized to the physical object distance r. For in-plane diffraction, the straight central groove is in the sagittal direction (normal to the meridional plane of incidence) and having a length coordinate $\ell$. This is the sum of the grating translation ($s$) and the illuminated aperture coordinate ($\sigma$) relative to a fixed point in space (P). By convention, the

Optics EXPRESS

meridional plane ($\omega - \hat{n}$ in Fig. 2) is designated as "horizontal" and the sagittal plane as "vertical", unrelated to the orientation of the physical instrument or the reader's perspective of the figures drawn in this paper. At a given scan wavelength (and thus translation), the horizontal aberration $\Delta x'$ is in the dispersion direction and is proportional to the fractional change in the meridional groove spacing $\mathrm{d}_\omega$ over the illuminated aperture $\Delta\sigma$. Furthermore, the vertical astigmatism aberration $\Delta z'$ is proportional to $\Delta\sigma$. Therefore, the image tilt angle $\psi' = \arctan\ (\Delta x'/\Delta z')$ is proportional to $[\Delta \mathrm{d}_\omega(\omega,\ell)/\mathrm{d}_\omega(\omega,\ell)]/\Delta\sigma$. To maintain a truly fixed geometry, this tilt angle (e.g. that of an exit slit) may not change as the grating is translated. This requires the 2D spacing function have the property that $\partial \mathrm{d}_\omega/\partial\ell \propto \mathrm{d}_\omega$:

$$\mathrm{d}_\omega(\omega,\ell) = \mathrm{e}^{c\ell}\,\mathrm{d}_\omega(\omega,0). \tag{1}$$

In the semi-classical case where $\mathrm{d}_\omega(\omega,0) = \mathrm{d}_\mathrm{o}$ (a constant), meridional integration of the density (1/d) is trivial, determining the groove number $N = \mathrm{e}^{-c\ell}\,\omega\,\mathrm{r}/\mathrm{d}_\mathrm{o}$. Thus, each groove is curved along the pure exponential $\omega(N,\ell) = \mathrm{e}^{c\ell}\,N\,\mathrm{d}_\mathrm{o}/\mathrm{r}$.

The exponential of Eq. (1) also provides equal changes to $\log(\lambda)$ per unit translation, facilitating a spectral scan over multiple octaves $q$. The exponential coefficient is:

$$c = (q/S)\ln 2 \tag{2}$$

where $S$ is the total translation. In the above equations, $\omega \equiv \mathrm{w}/\mathrm{r}$, $s \equiv \mathrm{s}/\mathrm{r}$ and $S \equiv \mathrm{S}/\mathrm{r}$ where w, s and S are physical dimensions. The required physical grating size is $2\breve{\omega}\mathrm{r}$ x $(S + 2\breve{\sigma})\mathrm{r}$, in which the sagittal dimension is the sum of the translation and the sagittal illumination $2\breve{\sigma}\mathrm{r}$ (typically << S).

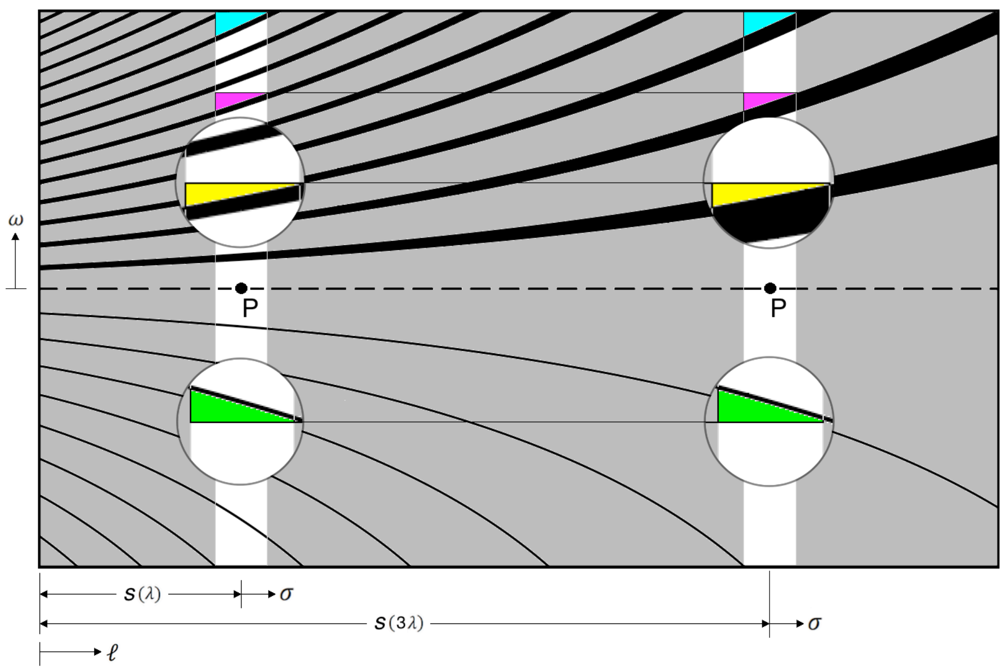


Fig. 1. A divergent groove grating, comprising an exponentially curved pattern. To scan wavelength, the grating translates by distance $s(\lambda)$ along its central groove (dashed), causing different regions (white) to be illuminated by a stationary incident beam centered on point P (fixed in space). At two sample positions of the scan, the color templates reveal 2D isotropy in the groove pattern; any geometrical aberration is thus fixed over the scan. A self-focusing version (shown here) also exhibits a variation in spacing with $\omega$. Though not affecting the focusing, the groove depth (exemplified by the black sidewalls of a triangular profile) is also shown scaling with the spacing. This option would extend the isotropy to 3D, providing a relative phase diffraction efficiency which is also independent of the scan wavelength.

Optics EXPRESS

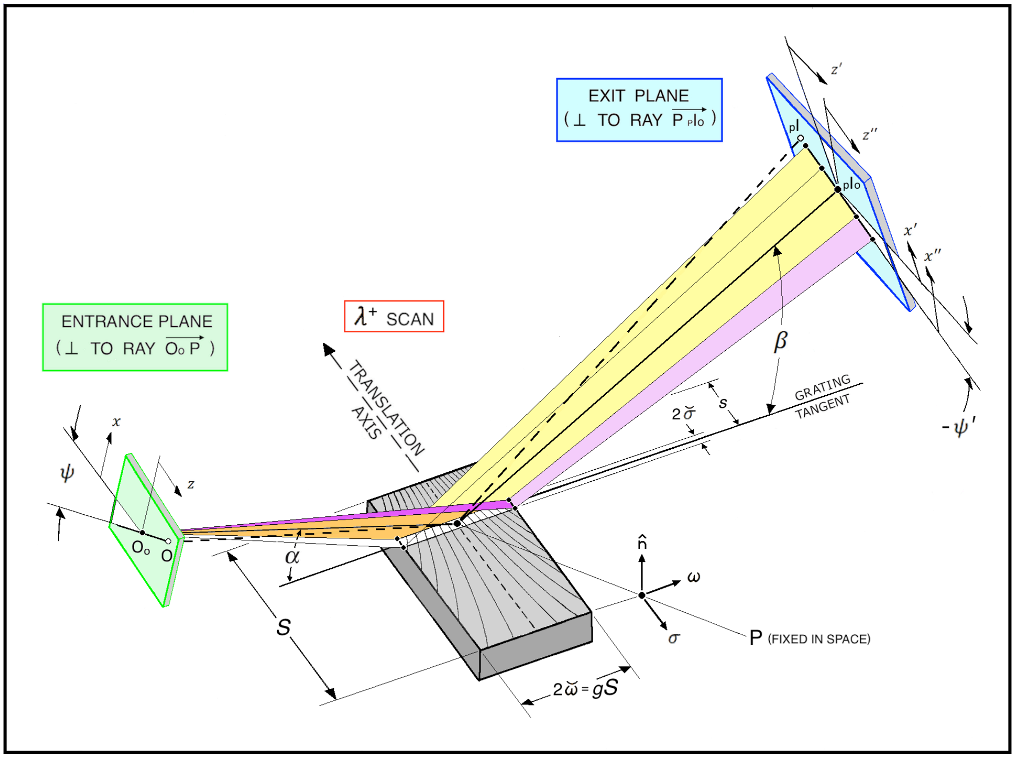


Fig. 2. A single-element divergent groove monochromator. A stationary iris (not shown) parallel to and positioned just above the grating surface provides illumination (white strip) fixed in space. In this self-focusing geometry, varied groove spacing in the meridional direction constrains $\Delta\lambda_{i0} = 0$ (all $i$), independent of the scan wavelength. The residual aberrations for plane and concave gratings at a grazing angle are given by Fig. 3, and their raytracings shown in Figs. 4 and 5, respectively. Non-grazing mountings are illustrated in Figs. 6 and 7. Plane gratings may employ a long entrance slit, as raytraced in Fig. 8. Note that the optically-defined "vertical" is in the direction of $z$ and $z'$ (see Sec. 2 of the text).

### 2.1 Two-dimensional varied line-space gratings

The aberration correction provided by one-dimensional varied line-space (VLS) gratings has previously been determined by expressing the groove number as a power series in the grating ruled width coordinate [1]. An extension of that formalism to two dimensions is given here as:

$$N(\omega,\sigma,s) = \frac{\mathrm{r}}{\mathrm{d}_\omega(0,0)} \sum_{i=0}^{n+1} \sum_{j=0}^{n-i+1} N_{ij}(s)\, \omega^i \sigma^j \tag{3}$$

where $N_{ij}$ are dimensionless coefficients, $N_{\mathrm{oo}}$ is an arbitrary number assigned to the groove passing through the origin and $n$ is the maximum value of the power-sum ($\equiv\ i + j - 1$). For the present divergent groove grating, expansion of Eq. (1) about the translation coordinate $s$ determines the full array of 2D coefficients over the (narrow) illuminated region $2\breve{\sigma}$ of the sagittal aperture, based on the 1D coefficients ($N_i$) in the meridional plane at $s = 0$:

$$N_{ij}(s) = N_i\, \mathrm{e}^{-cs}\, (-c)^j / j! \tag{4}$$

where $N_1 = 1$. Derivatives of Eq. (3) provide the groove density, locally measurable in the two directions and thus convenient for testing and raytracing:

$$\frac{1}{\mathrm{d}_\omega(\omega,\sigma)} = \frac{1}{\mathrm{r}} \sum_{i=0}^{\mathrm{n}} \sum_{j=0}^{\mathrm{n}-i} {}_\omega V_{ij}\ \omega^i \sigma^j \qquad \frac{1}{\mathrm{d}_\sigma(\omega,\sigma)} = \frac{1}{\mathrm{r}} \sum_{j=0}^{\mathrm{n}} \sum_{i=0}^{\mathrm{n}-j} {}_\sigma V_{ij}\ \omega^i \sigma^j \tag{5}$$

Optics EXPRESS

where the dimensionless density coefficients are ${}_\omega V_{ij} = (i+1)\, N_{i+1,j}$ and ${}_\sigma V_{ij} = (j+1)\, N_{i,j+1}$. Because they derive from the same scalar function ($N$), the "mixed" coefficients ($i \neq 0$ and $j \neq 0$) are related by ${}_\sigma V_{ij} = {}_\omega V_{i+1,j-1}\ (i+1)/j$.

As with prior 1D (straight and parallel groove) VLS gratings, any nonzero coefficients $N_i$ ($i > 1$) cause a meridional variation $\mathrm{d}_\omega(\omega)$. The 2D VLS spacing function $\mathrm{d}_\omega(\omega, \ell)$ is set by Eqs. (4) and (5) with the substitutions $j = 0$ and $\sigma = s = \ell$. Meridional integration of 1/d determines the groove number $N = \mathrm{e}^{-c\ell}(\mathrm{r}/\mathrm{d_o}) \sum_{i=1}^{n+1} N_i\ \omega^i$. The corresponding "varied exponential" curve of each groove is determined numerically, however including only the linear VLS coefficient ($N_2$) yields an accurate closed-form (quadratic) approximation:

$$\omega(N, \ell) \approx \left[\sqrt{1 + 4NN_2(\mathrm{d_o}/\mathrm{r})\, \mathrm{e}^{c\ell}} - 1\right] / (2N_2). \tag{6}$$

Expansion of the radical reveals that Eq. (6) reduces to the pure exponential in the limit of either a constant line-spacing ($N_2 = 0$) or as $\omega \to 0$ near the central groove ($N = 0$).

### 2.2 Grating fabrication

This novel grating design may be manufactured by existing maskless optical lithography systems (e.g. Heidelberg Instruments). These write unconstrained two-dimensional patterns over large apertures (150-1400 mm), such combination being unfeasible by the methods of mechanical ruling, interference lithography ("holography") or e-beam lithography. Blue lasers at 405 nm deliver a minimum feature size $\sim 500$ nm, allowing 1/d $\lesssim 1000$ g/mm; while frequency-doubled Argon lasers at 244 nm have produced 3000 g/mm gratings with features below 160 nm using nonlinear resists [7]. Though a tilt stage [8] also accommodates steeply curved (30 mm sag height) non-planar substrates, auto-focus of the piezo-driven objective in real time will follow the shallow meridional curvature required of the gratings proposed here (< 0.1 mm sag height) without compromising the feature size. Plane gratings manufactured by the maskless method may also be employed as masks in projection lithography systems developed for the manufacture of microprocessors. At present, immersion reduction at 193 nm (e.g. Cymer Inc.) delivers feature sizes below $100$ nm (1/d $\gtrsim 5000$ g/mm) on smaller (32 x 25 $\mathrm{mm}^2$) coherent plane apertures.

Optical lithography is not subject to the mechanical stresses of burnishing by a diamond tool, and maskless writing with lasers requires only minutes or hours (compared to days or months for mechanical rulings). This minimizes the groove positioning errors caused by environment variables (e.g. ground vibration, temperature and atmospheric pressure). Thus, given comparable systems for environmental isolation and interferometric control, the optically-written grating will exhibit smaller residual errors in the groove positions. Given a RMS random error $\Delta\mathrm{w_{RMS}}$, the fraction of diffracted intensity which is scattered in the dispersion direction as focused stray light ("grass") is [9]

$$FSL \approx (2\pi\, \Delta\mathrm{w_{RMS}}/\mathrm{d})^2. \tag{7}$$

The present commercially-available maskless pattern generators are equipped with translation and control systems suitable for the fabrication of integrated circuits (e.g. chip masks). Using the finest (10 nm) address grid for these systems, the $3\sigma$ specification for uniformity is 60 nm ($\Delta\mathrm{w_{RMS}} \sim 20$ nm). From Eq. (7), this will result in $FSL \lesssim 10^{-3}$ for groove spacings $\mathrm{d} > 4000$ nm $(1/\mathrm{d} < 250\ \mathrm{g/mm})$. Upgrading these sub-systems to the accuracy of $\Delta\mathrm{w_{RMS}} < 1$ nm achieved 40 years ago for mechanical ruling engines [10] will reduce the $FSL$ to $< 2.5 \times 10^{-6}$ at 250 g/mm, $4 \times 10^{-5}$ at 1000 g/mm and $2.5 \times 10^{-4}$ at 2500 g/mm.

Grooves of rectangular profile (mesa width = a; ravine width = d − a) and constant depth (h) require the fewest post-processing steps. *Amplitude diffraction* is realized if the ravines are optically inactive. This would occur if the bottom surface is non-reflective or (at grazing angles and short wavelengths) it is shadowed by the adjacent walls [$\mathrm{h/d} > (1 - \mathrm{a/d})/(1/\tan\alpha + 1/\tan\beta)$). Using Kirchoff theory, the $m$'th order relative diffraction efficiency is then

Optics EXPRESS

$$\varepsilon_m = [\sin(m\pi \, \mathrm{a}/\mathrm{d})/(m\pi)]^2. \tag{8}$$

In maskless lithography, both d and a may be specified as arbitrary functions of $\omega$ and $\ell$. For example, if $\mathrm{a}/\mathrm{d}$ is constant with $\ell$, then $\varepsilon_m$ is independent of the scan wavelength (as the grating translates by an amount $s$ along axis $\ell$, one has $\mathrm{a} \propto \mathrm{d} \propto \lambda \propto \mathrm{e}^{cs}$). In the case of $\mathrm{a}/\mathrm{d} = 0.5$, the nonzero even orders are eliminated and the odd orders provide $\varepsilon_m = 1/(m\pi)^2 = 0.101$ at $m = \pm 1$ and 0.011 at $m = \pm 3$. Note that Eq. (8) is also the efficiency of a transmission grating having gaps of width $\mathrm{a}$ between opaque bars of width $\mathrm{d} - \mathrm{a}$.

A more advanced option is to provide, independent of the scan wavelength, substantially higher first-order efficiency ($\varepsilon_1 \gtrsim 0.4$) by *phase diffraction*. This requires groove profiles of fixed aspect (h/d) along their lengths, representing an extension of isotropy to the third dimension. Varying the chemical etching time along parallel grooves (constant d) has previously provided a factor four continuous variation in the depth of a laminar profile [11]. However, the present divergent grooves require only a fixed h/d, which may be more accurately and readily formed as triangular profiles of constant blaze angle (e.g. at the lattice planes of a crystalline substrate). A further simplification is that the new scan method already translates the grating along the center groove, so no additional motion is needed.

## 3. Light-path analysis of a self-focused grating

The simplicity and high reflection efficiency of a single-element system are of particular advantages at short wavelengths and grazing incidence. In this section, geometrical parameters (including the 2D VLS coefficients) will be used to analytically express the aberrations for a monochromator based on a self-focusing divergent groove grating (Fig. 2). Detailed results for the spectral resolution of a plane grating will be given in Secs. 4 (grazing) and 6 (non-grazing). Sec. 5 will treat a concave grating surface.

The horizontal and vertical lateral ray coordinates at the Gaussian image plane are expanded as a sum of powers in grating aperture coordinates $(\omega, \sigma)$: $x'(\omega,\sigma) = \sum_{ij} x'_{ij} = \sum_{ij} {}_{ij}x' \, \omega^{i-1}\sigma^j$ and $z'(\omega,\sigma) = \sum_{ij} z'_{ij} = \sum_{ij} {}_{ij}z' \, \omega^i \sigma^{j-1}$.

The principal ray horizontal image coordinate ($x'_{10} = 0$) is fixed by the grating equation:

$$\mu \equiv m\lambda/\mathrm{d}(0,0) = \cos\beta - \cos\alpha \simeq 2\gamma^2(1-\rho)/(1+\rho) \tag{9}$$

where $\rho \equiv \sin\beta/\sin\alpha$. In this work, a small-angle approximation is preceded by the "$\simeq$" sign and is valid when the effective reflection graze angle $\gamma = (\alpha+\beta)/2$ is small.

The principal ray vertical image coordinate obeys the law of sagittal reflection, expressed here as $z'_{01} = -\eta \, z$, where $\eta \equiv \mathrm{r}'/\mathrm{r}$ is the image/object distance ratio for the principal ray.

### 3.1 General equations of a rigorous expansion method

The horizontal (${}_{ij}x'$) and vertical (${}_{ij}z'$) coefficients of the aberrant terms ($i + j - 1 > 0$) are provided by a mathematically consistent theory of light-path expansion [1,12]:

$${}_{ij}x' = -\eta \left\{ i\mu N_{ij} + \left[\partial A_{ij}/\partial(\Delta\omega) + \partial B_{ij}/\partial(\Delta\omega)\right]_{\omega^{i-1}\sigma^j \, coefficient} \right\} / \sin\beta \tag{10}$$

$${}_{ij}z' = \eta \left\{ j\mu N_{ij} + \left[\partial A_{ij}/\partial(\Delta\sigma) + \partial B_{ij}/\partial(\Delta\sigma)\right]_{\omega^{i}\sigma^{j-1} \, coefficient} \right\} \tag{11}$$

for which a circular cylinder (meridional concave radius $= R$), correct to power $\omega^6$, yields:

$$\partial A_{ij}/\partial(\Delta\omega) = \left[\cos\alpha - x_{ij}\sin\alpha + \left(R - \sin\alpha - x_{ij}\cos\alpha\right)b\right] / \sqrt{1 + {}_A t_{ij}} \tag{12}$$

$$\partial A_{ij}/\partial(\Delta\sigma) = \left(\sigma - z_{ij}\right) / \sqrt{1 + {}_A t_{ij}} \tag{13}$$

$$\partial B_{ij}/\partial(\Delta\omega) = \left[-\eta\cos\beta + \xi_{ij}\sin\beta + \left(R - \eta\sin\beta - \xi_{ij}\cos\beta\right)b\right] / \eta / \sqrt{1 + {}_B t_{ij}} \tag{14}$$

$$\partial B_{ij}/\partial(\Delta\sigma) = \left(\sigma - \zeta_{ij}\right) / \eta / \sqrt{1 + {}_B t_{ij}} \tag{15}$$

Optics EXPRESS

where $b = [(\omega/R) + (\omega/R)^3/2 + 3(\omega/R)^5/8]$ is the surface slope at $\omega$. For a plane grating, the last product in the numerators of Eqs. (12) and (14) simplifies to $\omega$. The Taylor series for $1/\sqrt{1+t}$ is $1 - t/2 + 3t^2/8 - 5t^3/16 + 35t^4/128 + \cdots$. Correct to power $\omega^7$, the lateral squared distances ($t$) are:

$$ {}_At_{ij} = 2\omega(\cos\alpha - x_{ij}\sin\alpha) - 2z_{ij}\sigma + x_{ij}^2 + z_{ij}^2 + \sigma^2 + 2(R - \sin\alpha - x_{ij}\cos\alpha)\cup \tag{16}$$

$$ {}_Bt_{ij}\eta^2 = 2\omega(\xi_{ij}\sin\beta - \eta\cos\beta) - 2\zeta_{ij}\sigma + {\xi_{ij}}^2 + {\zeta_{ij}}^2 + \sigma^2 + 2(R - \eta\sin\beta - \xi_{ij}\cos\beta)\cup \tag{17}$$

where $\cup = \omega[(\omega/R)/2 + (\omega/R)^3/8 + (\omega/R)^5/16]$ is the depth of the pole relative to the surface at $\pm\omega$. For a plane grating, the last product in Eqs. (16) and (17) simplifies to $\omega^2$. The reference image coordinates $\xi_{ij}$ and $\zeta_{ij}$ include all (paraxial and non-paraxial) power terms except those of the subject aberration ($x'_{ij}$ and $z'_{ij}$):

$$\xi_{ij} = \sum_{\substack{(I,J)\\ \neq(i,j)}} x'_{IJ} = \sum_{\substack{(I,J)\\ \neq(i,j)}} {}_{IJ}x'\,\omega^{I-1}\sigma^J \quad \text{and} \quad \zeta_{ij} = \sum_{\substack{(I,J)\\ \neq(i,j)}} z'_{IJ} = \sum_{\substack{(I,J)\\ \neq(i,j)}} {}_{IJ}z'\,\omega^{I}\sigma^{J-1}. \tag{18}$$

Numerical raytracings show that a sphere results in negligible change to the grating aberrations at grazing angles, however the above light-path equations employ a meridional cylinder on which the central groove remains straight in the translation (sagittal) direction.

### *3.2 Explicit expansion terms for a point object*

Given $x_{ij} = z_{ij} = 0$ (a point object in the meridional plane), consider the 18 coefficients (${}_{ij}x'$ and ${}_{ij}z'$) for which $i + j - 1 = 1$, 2 or 3. Due to the in-plane geometry of the present grating design, ${}_{0j}z' = 0$ for all odd values of $j$, including ${}_{03}z'$. Also, numerical raytrace extractions determined the coefficients ${}_{22}x', {}_{13}z', {}_{13}x'$ and ${}_{04}z'$ to be negligible ($\sim 10^{-8}$). Equations (10)-(18) were used to derive the remaining 13 coefficients, employing substitute variables ${}_{ij}T \equiv {}_{ij}x'\sin\beta/(\mu\,\eta)$, $\tau \equiv \cos\beta$, $\Gamma \equiv \cos\alpha/\cos\beta$, $Q \equiv \mu/\sin^2\beta$ and $\kappa \equiv R\sin\beta$. Note that $\tau \simeq \Gamma \simeq 1$ at grazing incidence ($\alpha, \beta \ll 1$) and $Q$ is of order unity at all angles:

$$ {}_{02}z'/\eta = 1 + 1/\eta \tag{19}$$

$$ {}_{11}T = c \tag{20}$$

$$ {}_{11}z'/\eta = -c\mu \tag{21}$$

$$ {}_{20}T = \left(\frac{1}{\kappa} + \frac{1}{\kappa\rho} - \frac{1}{\rho^2} - \frac{1}{\eta}\right)\frac{1}{Q} - 2N_{20} \tag{22}$$

$$ {}_{12}z'/\eta = -(\Gamma + 1/\eta)\tau + c^2\mu \tag{23}$$

$$ {}_{21}T = \left[2N_{20}(1 + Q\tau) + \left(1 - \frac{1}{\eta} + \frac{1}{\rho^2} - \frac{1}{\rho\kappa}\right)\tau\right]c \tag{24}$$

$$ {}_{21}z'/\eta = (\tau/\eta - N_{20})c\mu \tag{25}$$

$$ {}_{30}T = -3N_3 + \left\{\left[\left(\frac{1}{\eta} - \frac{\Gamma}{\rho}\right)\frac{1}{\kappa} - \left(\frac{1}{\eta^2} - \frac{\Gamma}{\rho^2}\right)\right]\frac{3}{Q} + \left[\left(\frac{2}{\kappa} - \frac{4}{\eta}\right){}_{20}T - Q\,{}_{20}T^2 - c^2\mu\right]\right\}\frac{\tau}{2} \tag{26}$$

$$ {}_{12}T = -[1 + (1 + Q\,\tau)\,c^2]/2 \tag{27}$$

$$ \frac{{}_{31}z'}{\eta} = \left(\frac{\tau}{\eta}N_{20} - N_{30}\right)c\mu + \left\{\left(\frac{1}{\eta\kappa} - \frac{1}{\eta^2}\right)\frac{1}{2Q} - \left[\frac{{}_{20}T}{\eta} + \frac{Q}{2}\,{}_{20}T^2\right]\right\}c\mu^2 - \frac{c^3\mu^3}{2} \tag{28}$$

$$ {}_{40}T = -\left\{4N_{40} + \left[\left(\frac{1}{\eta^3} + \frac{1}{\rho^2}\right) - \frac{5}{4}\left(\frac{1}{\eta^3} + \frac{1}{\rho^4}\right)\sin^2\beta\right]\frac{2}{Q}\right\}$$

Optics EXPRESS

$$+\left\{\left[\left(\frac{1}{\eta^2}+\frac{1}{\rho}\right)-\frac{3}{2}\left(\frac{1}{\eta^2}+\frac{1}{\rho^3}\right)\sin^2\beta\right]\frac{2}{\kappa}-\left(\Gamma^2+\frac{1}{\eta}\right)\frac{\tau^2}{2\kappa^2}+\left(1+\frac{1}{\rho}\right)\frac{\sin^2\beta}{2\kappa^3}\right\}\frac{1}{Q}$$

$$-\left[\left(\frac{3}{\eta^2}-\frac{3}{2\eta\kappa}\right){}_{20}T+\frac{Q}{\eta}{}_{20}T^2+\left(\frac{2}{\eta}-\frac{1}{\kappa}+{}_{20}TQ\right){}_{30}T\tau\right]$$

$$+\left[\left(\frac{9}{\eta}-\frac{6}{\kappa}\right)\frac{{}_{20}T}{\eta Q}+\left(\frac{5}{\eta}-\frac{1}{\kappa}\right){}_{20}T^2+Q\,{}_{20}T^3-2N_{20}\tau c^2\right]\frac{\mu}{2}+\left({}_{20}T+\frac{1/\eta-1/\kappa}{Q}\right)\frac{c^2\mu^2}{2} \quad (29)$$

$$\frac{{}_{22}z'}{\eta}=\left(1+\frac{\Gamma}{\eta}\right)+\left(N_{20}-\frac{\tau}{\eta}\right)c^2\mu+\left[\left(\frac{1}{\eta^2}+\frac{1}{\rho\kappa}-\frac{1}{\eta\kappa}-\frac{3}{\rho^2}-\frac{2}{\eta}\Gamma\right)\frac{1}{2Q}+\left(\frac{3}{2}-\frac{1}{\eta}\right)c^2\mu\right]\mu$$

$$+\left(\frac{{}_{20}T}{\eta}+\frac{Q}{2}{}_{20}T^2\right)\mu-{}_{20}TQc^2\mu^2 \quad (30)$$

$${}_{31}T=\left[3N_{30}+N_{20}\tau-\Gamma+\frac{3}{2\eta^2}\left(\frac{\eta}{\kappa}-2\right)-\frac{2}{\eta}{}_{20}TQ-{}_{30}TQ\tau\right]c+{}_{21}T\left(\frac{1}{\kappa}-\frac{2}{\eta}-{}_{20}TQ\right)\tau$$

$$+\left\{\tau c^2+\left[\frac{3}{\eta^2}\left(\frac{3}{2}-\frac{\eta}{\kappa}\right)+\Gamma+\frac{1}{\kappa}-\frac{1}{\eta}\right]\frac{1}{Q}+\left(\frac{5}{\eta}-\frac{1}{\kappa}-1\right){}_{20}T+\frac{3}{2}{}_{20}T^2Q\right\}c\mu+\frac{c^3\mu^2}{2}. \quad (31)$$

These horizontal ($x'$) and vertical ($z'$) image plane positions of a monochromatic ray are projected to the spectral direction ($x''$), oriented at an angle $\psi'$ from the horizontal (see Secs. 3.3 and 3.4). The modulus of the full variation in this direction, as the rays wander over the rectangular illuminated grating aperture ($\omega = \pm\breve{\omega}$, $\sigma = \pm\breve{\sigma}$) is the extremum ($\Delta$) aberration:

$$\Delta x''_{ij} = \left|\left({}_{ij}x'\cos\psi' - {}_{i-1,j+1}z'\sin\psi'\right)\right| p_{ij}(2\breve{\omega})^{i-1}(2\breve{\sigma})^j \quad (32)$$

where $p_{ij} = 2^{1-(i+j)}$ if $i$ is odd and $j$ is even (otherwise $p_{ij} = 2^{2-(i+j)}$). Differentiation of Eq. (9) converts this spatial aberration to wavelength at the principal ray position ($x'' = 0$):

$$\Delta\lambda_{ij}/\lambda = \left(\Delta x''_{ij}/\cos\psi'\right)(\sin\beta)/\eta/\mu. \quad (33)$$

In the perpendicular direction, the extremum aberration is:

$$\Delta z''_{ij} = \left|\left({}_{ij}z'\cos\psi' + {}_{i+1,j-1}x'\sin\psi'\right)\right| p_{ji}(2\breve{\omega})^{i}(2\breve{\sigma})^{j-1}. \quad (34)$$

### *3.3 Horizontal image tilt (sagittally-induced)*

The lowest-degree mixed horizontal aberration created by the exponential groove pattern is $x'_{11}$, resulting from the nonzero value of $N_{11} = -c$ in Eq. (4). Due to the linearity of $x'_{11}$ with the sagittal pupil coordinate $\sigma$, this is simply a tilt of the astigmatic image by the angle $\psi'_s = \arctan\,(x'_{11}/z'_{02})$ relative to the horizontal. From Eqs. (19) and (20):

$$\tan\psi'_s = \frac{c\,\mu}{(1+1/\eta)\sin\beta} \quad (35)$$

where a positive value is counter-clockwise for an upstream observer. Therefore, the projection of these two aberrations in the spectral direction ($x''_{11} = x'_{11}\cos\psi' - z'_{02}\sin\psi'$) is made zero by use of an exit slit oriented at the fixed angle $\psi' = \psi'_s$. In Fig. 2, a vertical sheet of incident rays (magenta) strikes the far edge of the illuminated rectangular aperture, at meridional coordinate $\omega = +\breve{\omega}$. Upon diffraction (lighter magenta), this sheet of rays rotates clockwise to the angle $\psi'$, measured within the exit plane.

### *3.4 Vertical image tilt (meridionally-induced)*

The lowest-degree mixed vertical aberration ($z'_{11}$) would extend a perfect horizontal focus for meridional rays ($x'_{20} = 0$) into a vertical line. This would be viewed by the tilted slit as a

Optics EXPRESS

defocus normal to its length (multiplied by $\tan\psi'_{\rm s}$). In effect, the vertical aberration from the meridional rays induces a second tilt angle $\psi'_{\rm m} = \arctan(x'_{20}/z'_{11})$. From Eqs. (21) and (22):

$$\tan\psi'_{\rm m} = \left[2N_{20} + \left(\frac{1-\rho/\kappa}{\rho^2} + \frac{1-\eta/\kappa}{\eta}\right)\frac{1}{Q}\right]/(c\,\sin\beta). \tag{36}$$

The solution is to purposely “defocus” the grating horizontally to force equality of the two tilts, as geometrically illustrated in Fig. 2. A horizontal sheet of incident rays (orange) strikes the grating at sagittal coordinate $\sigma = -\breve{\sigma}$ (left edge of the illuminated rectangular aperture). The diffracted sheet of rays (yellow) rotates counter-clockwise to the same tilt angle as given in Sec. 3.3 for the vertical (magenta) rays. Algebraically, this requires a simultaneous solution of Eqs. (35) and (36), yielding exact cancellation of spectral defocusing ($0 = x''_{20} = x'_{20}\cos\psi' - z'_{11}\sin\psi'$). This is provided by the first-power VLS coefficient:

$$2N_{20} = -\left(\frac{1-\rho/\kappa}{\rho^2} + \frac{1-\eta/\kappa}{\eta}\right)\frac{1}{Q} + \frac{c^2\mu}{1+1/\eta} \tag{37}$$

where the term in $c^2\mu$ is effectively a correction for the sagittally-induced tilt of Eq. (35). Likewise, canceling the next higher-power aberration of “meridional coma” in the spectral direction ($0 = x''_{30} = x'_{30}\cos\psi' - z'_{21}\sin\psi'$) determines the second-power VLS coefficient:

$$3N_{30} = \frac{\tau}{2}\left\{\left(\frac{1}{\eta\kappa} - \frac{\Gamma}{\rho\kappa} - \frac{1}{\eta^2} + \frac{\Gamma}{\rho^2}\right)\frac{3}{Q} + {}_{20}T\left(\frac{2}{\kappa} - \frac{4}{\eta}\right) - {}_{20}T^2 Q + \left[2\frac{\eta N_{20} - \tau}{(\eta+1)\tau} - 1\right]c^2\mu\right\}. \tag{38}$$

Cancelation of “spherical aberration” in the spectral direction ($0 = x''_{40} = x'_{40}\cos\psi' - z'_{31}\sin\psi'$) determines the third-power VLS coefficient:

$$\begin{aligned}4N_{40} = {} & \left[\frac{1}{\eta^2\kappa} + \frac{1}{\rho\kappa} - \frac{2}{\eta^3} - \frac{2}{\rho^2} - \left(\frac{1}{\eta^2\kappa} + \frac{1}{\rho^3\kappa} - \frac{1}{\eta^3} - \frac{1}{\rho^4} - \frac{1}{\kappa^3} - \frac{1}{\rho\kappa^3}\right)\frac{\tan^2\beta}{2} - \frac{1/\eta + \Gamma^2}{2\kappa^2}\right]\frac{\tau^2}{Q} \\ & - \left[\left(\frac{6}{\eta} - \frac{3}{\kappa}\right)\frac{{}_{20}T}{2\eta} + \frac{{}_{20}T^2 Q}{\eta} + \left(\frac{2}{\eta} - \frac{1}{\kappa} + {}_{20}TQ\right){}_{30}T\tau\right] \\ & + \left[\frac{N_{30} - (1+2/\eta)N_{20}\tau}{1+1/\eta}(2c^2) + \left(\frac{9}{\eta} - \frac{6}{\kappa}\right)\frac{{}_{20}T}{\eta Q} + \left(\frac{5}{\eta} - \frac{1}{\kappa}\right){}_{20}T^2 + {}_{20}T^3 Q\right]\frac{\mu}{2} \\ & + \left[\left(\frac{1}{\eta} - \frac{1}{\kappa}\right)\left(1 + \frac{2}{\eta}\right)\frac{1}{Q} + \left(1 + \frac{3}{\eta}\right){}_{20}T + {}_{20}T^2 Q\right]\frac{c^2\mu^2}{2(1+1/\eta)} + \frac{c^4\mu^3}{2(1+1/\eta)}.\end{aligned} \tag{39}$$

Numerical raytracings confirm that Eqs. (37)-(39) result in removal of the $x''_{20}$, $x''_{30}$ and $x''_{40}$ lateral ray aberrations (numerical residuals $< 10^{-13}$ radians). This cancelation may continue for indefinitely high powers of the pure meridional aberrations, to obtain $\Delta\lambda_{i0} = x''_{i0} = 0$ for all *i*. In general, if $x''_{ij} = 0$, the following condition is noted from Eqs. (32) and (35):

$${}_{ij}T = \left({}_{\rm i-1,j+1}{\rm z}'/\eta\right)\,c\,/(1+1/\eta). \tag{40}$$

## 4. Residual spectral aberrations of a grazing incidence plane grating

### *4.1 Bowtie aberration ($\Delta\lambda_{21}$)*

The above removal of $\Delta\lambda_{11}$ and $\Delta\lambda_{i0}$ leaves $\Delta\lambda_{21}$ as the dominant spectral aberration. Using Eqs. (23), (24), (32) and (33), and substituting $2\breve{\omega} = \phi_{\rm m}/\sin\alpha$, $2\breve{\sigma} = \phi_{\rm s}$ and $c = (q/S)\ln 2$, this aberration is expressed in parameters related to performance and construction, including the solid angle of collection ($\Omega = \phi_{\rm m}\phi_{\rm s}$) from the object:

Optics EXPRESS

$$\frac{\Delta\lambda_{21}}{\lambda} = \left| 2(1+Q\tau)N_{20} + \left(1 - \frac{1}{\eta} + \frac{1-\rho/\kappa}{\rho^2}\right)\tau + \frac{(\Gamma + 1/\eta)\tau - c^2\mu}{1+1/\eta} \right| \frac{q}{S} \frac{\Omega}{\sin\alpha} \frac{\ln 2}{2}. \quad (41)$$

A planar surface $(\kappa = \infty)$ simplifies the grating fabrication and exhibits a focal length $(\eta)$ which is nearly independent of $\gamma \lesssim 15^{\text{o}}$ at fixed $\rho$ [1, Secs. 2.4 and 8.8.5]. At these grazing angles, the approximations $\tau \simeq \Gamma \simeq 1$ , $\mu \ll 1$ , $Q \simeq (1/\rho^2 - 1)/2$ , $N_{20} \simeq (\rho^2/\eta + 1)/(\rho^2 - 1)$ and $\sin\alpha \simeq \alpha \simeq 2\gamma/(\rho + 1)$ further simplify Eq. (41):

$$\left(\frac{\Delta\lambda_{21}}{\lambda}\right)_{\text{sep}} \simeq \left| \frac{\rho^2 + 1/(M\rho)}{(\rho - 1)(1 + M\rho)} \right| \frac{\text{L}}{\text{S}} \frac{\Omega q}{\sin\gamma} \frac{\ln 2}{2} f_{21} \quad (42)$$

where $M = \eta/\rho$ converts $\eta$ to a performance parameter (the grating horizontal magnification) and $\text{L} = (1+\eta)\ \text{r}$ is the object-to-image path-length. Note that $\rho$, geometrically defined as $\sin\beta/\sin\alpha$ [e.g. see Eq. (9)], is also the relative diffraction efficiency (or its reciprocal if $\rho > 1$) of a blazed triangular groove. The "sep" subscript denotes this is a measure of marginal resolution, defined as the center-to-center separation of a doublet whose scan profile exhibits a dip of 25%. This requires a form factor $f_{21}$, which depends on the horizontal aberration $(i = 2, j = 1)$ and the width of the exit slit. Numerical raytracings find $f_{21}{\sim}1/3$ if the exit slit width transmits half of the intensity at either peak.

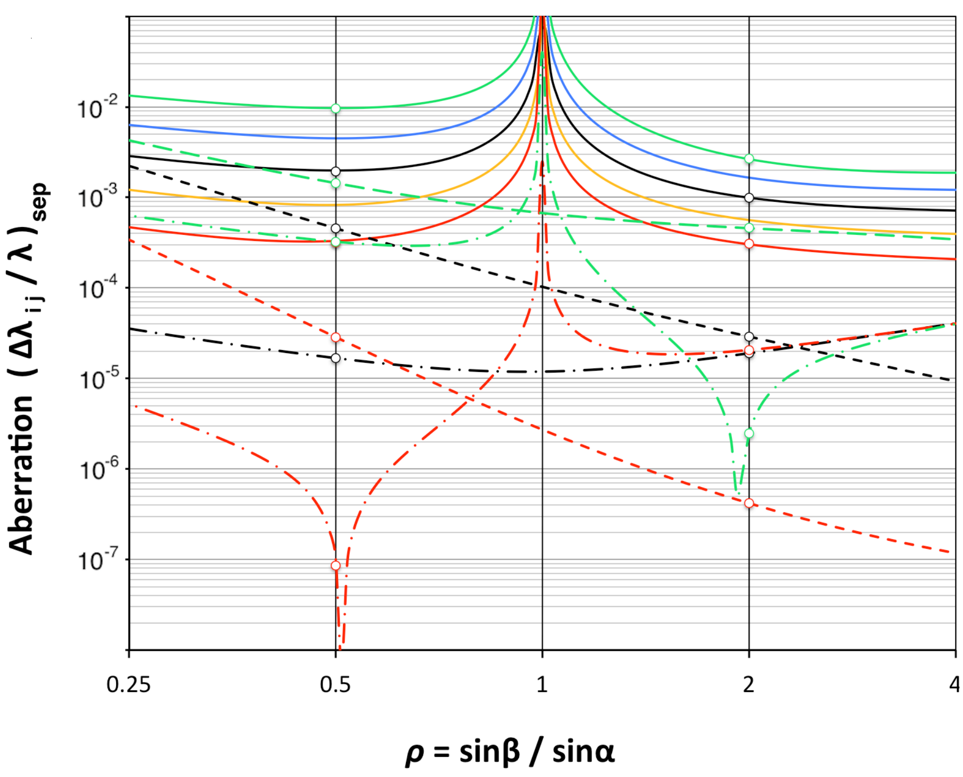


Fig. 3. Geometrical aberrations at the exit plane of a self-focused divergent groove grating at a 3° graze angle. Due to the fixed geometry, all aberrations are independent of the scan wavelength. The object is a point and the detailed parameters are given in the text. Curves are light-path calculations of the dominant terms for a plane grating ($\Delta\lambda_{21}/\lambda$, solid) and a concave grating ($\Delta\lambda_{12}/\lambda$, dash and $\Delta\lambda_{31}/\lambda$, dot-dash). Horizontal magnification is ¼ (green), ½ (blue), 1 (black), 2 (orange) and 4 (red). Precise extractions from numerical raytracings (open circles) match the light-path curves to approximately 13 decimal digits.

Consider a small monochromator (L = 500 mm, S = 40 mm) scanning $q$ = 3 octaves in the soft x-ray at $\gamma = 3^{\text{o}}$ and $\Omega = 8 \text{ x } 10^{-6}$. The solid curves in Fig. 3 plot Eq. (42) at different magnifications ($M$) and as a continuous function of $\rho$. The aberration is near local minima at $\rho \sim 1/2$ and $\rho \sim 2$, where numerical raytrace extraction data (Sec. 4.2) are plotted at several magnifications, providing independent confirmation of the light-path calculations to within the software accuracy (64-bit). At $M = 1$ and $\rho = 2$, $(\Delta\lambda_{21}/\lambda)_{\text{sep}} \sim 10^{-3}$, with other parameters as follows: $\eta = 2$, $\alpha = 2^{\text{o}}$, $\beta = 4^{\text{o}}$, $m = -1$, $\mu = 0.0018283$, $\text{r} = 166.67$ mm, $\text{r}' = 333.33$ mm, $c = 8.664$ and $\psi' = -8.607^{\text{o}}$.

### *4.2 Numerical raytracings of a compact soft x-ray monochromator*

The above light-path equations have been verified by the independent calculations of numerical raytracing, employing a recent 2D enhancement of the VLS coefficients included in the open source code BEAM4 [13]. In particular, the basis Eqs. (19)-(31) agree exactly with the results of the numerical raytrace extraction method given by equations (75)-(83) and (86) in a recent paper [1]. The discrepancies are < $10^{-13}$ radians, corresponding to a lateral image size error of < 0.001 nm at a grating focal length of 10 meters. This sub-atomic scale is many orders of magnitude smaller than the diffraction limit of soft x-rays.

In the case of the mixed aberrations given by Eqs. (23), (24), (30) and (31), the 21-ray extraction method (see Sec. 7.3 in [1]) initially confirmed their accuracy to $10^{-11}$~$10^{-12}$ radians. This was improved to $10^{-13}$~$10^{-14}$ radians (comparable to the 64-bit floating point accuracy of the software) by adding the following rays: $21\left(\frac{1}{4}\breve{\omega}, \frac{1}{4}\breve{\sigma}\right)$, $22\left(-\frac{1}{4}\breve{\omega}, \frac{1}{4}\breve{\sigma}\right)$, $23\left(-\frac{1}{4}\breve{\omega}, -\frac{1}{4}\breve{\sigma}\right)$ and $24\left(\frac{1}{4}\breve{\omega}, -\frac{1}{4}\breve{\sigma}\right)$. Using this enhanced (25-ray) extraction, the equations

$$\Delta z'_{12} = \frac{1}{90}\left[\left(z'^{9-}_{10} + z'^{11-}_{12}\right) - 80\left(z'^{17-}_{18} + z'^{19-}_{20}\right) + 1024\left(z'^{21-}_{22} + z'^{23-}_{24}\right)\right] \tag{43}$$

$$\Delta x'_{21} = \frac{1}{90}\left[\left(x'^{9-}_{10} + x'^{11-}_{12}\right) - 80\left(x'^{17-}_{18} + x'^{19-}_{20}\right) + 1024\left(x'^{21-}_{22} + x'^{23-}_{24}\right)\right] \tag{44}$$

for the 2nd power mixed terms remove contamination by the 6th power mixed terms, and

$$\Delta z'_{22} = \frac{1}{90}\left[\begin{pmatrix} z'^{9-}_{12} + z'^{10-}_{11} \\ -2z'^{6-}_{8} \end{pmatrix} - 160\begin{pmatrix} z'^{17-}_{20} + z'^{18-}_{19} \\ -2z'^{2-}_{4} \end{pmatrix} + 4096\begin{pmatrix} z'^{21-}_{24} + z'^{22-}_{23} \\ -2z'^{14-}_{16} \end{pmatrix}\right] \tag{45}$$

$$\Delta x'_{31} = \frac{1}{90}\left[\begin{pmatrix} x'^{9-}_{12} + x'^{10-}_{11} \\ -2x'^{6-}_{8} \end{pmatrix} - 160\begin{pmatrix} x'^{17-}_{20} + x'^{18-}_{19} \\ -2x'^{2-}_{4} \end{pmatrix} + 4096\begin{pmatrix} x'^{21-}_{24} + x'^{22-}_{23} \\ -2x'^{14-}_{16} \end{pmatrix}\right] \tag{46}$$

for the 3rd power mixed terms remove contamination by the 7th power mixed terms.

If the small monochromator described in Sec. 4.1 has a square grating format (aspect $g$ = 1) of 40 mm x 40 mm, then $\phi_{\text{m}} =$ 8.4 mrad and $\phi_{\text{s}} =$ 0.96 mrad. However, the solid angle and hence the spectral resoluton are unchanged if $\phi_{\text{m}}$ is decreased and $\phi_{\text{s}}$ increased in proportion. For example, $\phi_{\text{m}} =$ 2.83 mrad and $\phi_{\text{s}} =$ 2.83 mrad reduces the grating meridional dimension to 13.5 mm ($g$ = 0.3375). Though the vertical astigmatism ($\Delta z'_{02}$) triples, this does not significantly increase the overall image length, due to the $\Delta z'_{11}$ aberration component having been comparable and is now reduced by a factor of 3. In fact, the 2D image brightness increases downstream of the exit slit [Fig. 4(c)], due to the reduced angular aperture in the horizontal direction. It is noted that the fewer number of grooves illuminated is not an issue for this moderate resolution design, as only a few thousand are required on the basis of physical diffraction (see Eq. (66)). An elliptical iris (13.5 mm x 0.47 mm $\simeq$ 2.83 mrad x 2.83 mrad) is used to remove the most offensive (21.5%) rays at the corners of the rectangular region shown in Fig. 2. Figure 4(a) shows the 2D spot diagram (on the exit plane) of a point object whose spectral output consists of a line doublet. Figure 4(b) is a wavelength scan, where the indicated intensity values are the geometrically-transmitted fraction (through iris and exit slit) of the photons emitted by the object over a solid angle of

Optics EXPRESS

$8 \times 10^{-6}$ sr at each of the two (equal strength) lines. The 26.5% dip in the transmitted intensity between these lines is slightly better than that of the standard Rayleigh criterion, and confirms the marginal resolution of $(\Delta\lambda_{21}/\lambda)_{\mathrm{sep}} = 10^{-3}$ plotted in Fig. 3 from Eq. (42).

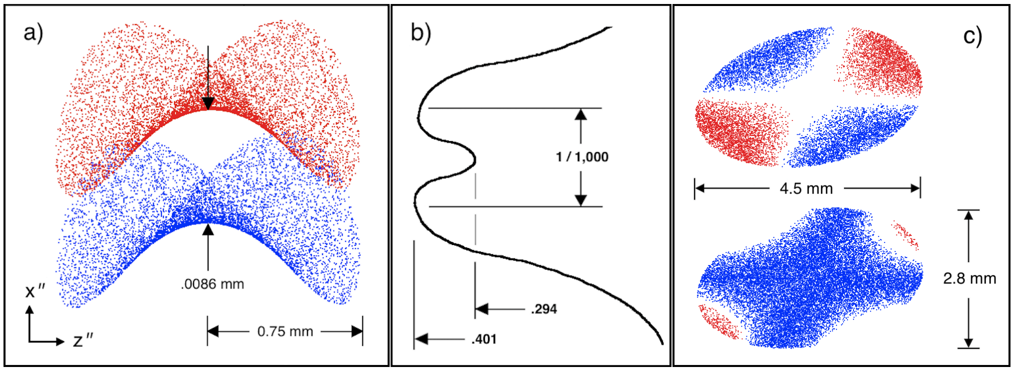


Fig. 4. Numerical raytracings of a self-focused divergent groove plane grating at a $3^{\mathrm{o}}$ graze angle. The monochromator length is 0.5m, the magnification is unity, $\rho = 2$, and $\phi = 0.00283$. Given a spectral scan of 3 octaves (e.g. $\lambda =$ 1 - 8 nm), the grating size is 13.5 mm x 40 mm and is illuminated by a 13.5 mm x 0.47 mm ellipse. a) The red and blue images shown at the exit slit plane are for a point object emitting two wavelengths separated by 1 part in 1,000. b) The scan intensity profile shows these lines are marginally resolved (26.5% dip), including a 0.004 mm object width and a 0.004 mm width straight exit slit. At either peak, $3.2 \times 10^{-6}$ sr of that line radiation from the object is geometrically transmitted. c) Image 1 m downstream of the monochromator, tuned to the dip (upper) or to the blue line peak (lower).

For a minimum physical wavelength of 1 nm, the groove density is 1828/mm near one end of the sagittal dimension and decreases by the required 3 octaves (factor of 8) to 228/mm over the translation range of 40 mm (for a maximum wavelength of 8 nm). As there need not be coherence over more than the illuminated groove length (0.472 mm), the grating may be assembled from three square segments. each 13.5 mm x 13.5 mm and covering one octave. Alternatively, an array of 7 such sub-gratings can scan the entire grazing incidence region extending from ~ 0.75 nm in the deep soft x-ray to 96 nm at the border of the far ultraviolet.

Doubling S/L (to 1/6.25) in Eq. (42) would halve the limiting aberration (to 1/2000). The slit widths required by Eq. (65) would remain unchanged if the length of the monochromator was also doubled (to L = 1000 mm). The grating size would increase to 27 mm x 160 mm (or five individually coherent segments produced by DUV projection lithography, each 27 mm x 32 mm) with an elliptical illumination of 27 mm x 0.94 mm. At the same grating format, illumination and slit widths, each subsequent 2-fold improvement in spectral resolution requires a 2-fold increase in the length and a 4-fold decrease in the solid collection angle.

## 5. Residual spectral aberrations of a grazing incidence concave grating

### *5.1 Cancelation of the bowtie aberration ($\Delta\lambda_{21}$)*

The dominant aberration of the above plane grating may be eliminated by use of a meridionally-concave surface (e.g. a cylinder or sphere). The required curvature is obtained by setting Eq. (41) to zero:

$$\frac{1}{\kappa} = \frac{(1/\rho^2 + 1/\eta)(1 + 1/\eta) + (2/\eta^2 - \Gamma - 1)Q\tau - Q^2 c^2 \mu}{(1 + 1/\rho + Q\tau)(1 + 1/\eta)}$$

$$\simeq 2\frac{\rho^2 + 1/\eta}{(\rho + 1)^2} - \frac{(1 - 1/\rho)^2}{2(1 + 1/\eta)} c^2 \mu \qquad (47)$$

which is verified by numerical raytracings to cancel $\Delta\lambda_{21}$ (within the 64-bit calculation accuracy of $\sim 10^{-13}$ radians). Because $\Delta\lambda_{20}$, $\Delta\lambda_{30}$ and $\Delta\lambda_{40}$ were already eliminated (Sec. 3.4), the only spectral aberrations remaining to a power-sum $\leq 3$ are $\Delta\lambda_{12}$ and $\Delta\lambda_{31}$.

In the case of unit magnification ($\eta = \rho$), the small-angle approximation reveals $\kappa \simeq \eta/2$ at $\rho = 2$ (inside order) and $\kappa \simeq \eta$ at $\rho = 1/2$ (outside order). Thus, the outside order results in twice the radius of curvature, of practical benefit in forming the grating groove profile. The condition $\kappa = \eta = \rho$ corresponds to horizontal focusing on the Rowland circle [14], for which Eqs. (37) and (38) confirm the VLS coefficients $N_{20}$ and $N_{30}$ are nearly zero. Their residuals ($\propto \mu$) arise from the nonzero values of the vertical aberrations ${}_{11}z'$ and ${}_{21}z'$ in Eqs. (21) and (25). From Eq. (32), these project in the direction of the tilted image width, thus contributing to ${}_{20}x''$ and ${}_{30}x''$, albeit an increasingly small amount at grazing angles. This divergent groove grating may replace the classical one in a Rowland circle spectrometer, resulting in wavelength scanning by sagittal translation of the grating. In this configuration, the exit slit would be fixed (though tilted relative to the classical case) and the object would also be fixed (though not be an extended slit, per the discussion in Sec. 7.2).

### *5.2 Astigmatic curvature aberration ($\Delta\lambda_{12}$) and exit slit curvature*

Equations (27), (32) and (33) determine this 2nd power extremum wavelength aberration:

$$\frac{\Delta\lambda_{12}}{\lambda} = |[(1 + Q\,\tau)\,c^2] + 1|\,\frac{(2\breve{\sigma})^2}{8} \tag{48}$$

which is in exact agreement ($\sim 10^{-13}$ radians) with numerical raytrace extractions given by Eqs. (80) and (86) of a recent paper [1]. The small angle approximation yields:

$$\left(\frac{\Delta\lambda_{12}}{\lambda}\right)_{\mathrm{sep}} \simeq \left\{\left[\left(\frac{1}{\rho^2}+1\right)\frac{c^2}{2}\right]+1\right\}\frac{{\phi_s}^2}{8}f_{12}$$

$$\simeq \left\{\left[\frac{2+2\rho+2/\rho+\rho^2+1/\rho^2}{(1+M\rho)^4}\right]\left(\frac{\ln 2}{8}\right)^2+\frac{(\rho+1)^2/(1+M\rho)^2}{32\,q^2(\mathrm{L/S})^2}\right\}\left(\frac{\mathrm{L}^2\,\Omega\,q}{g\mathrm{S}^2\sin\gamma}\right)^2 f_{12}. \tag{49}$$

The solid collection angle ($\Omega$), the graze angle ($\gamma$) and the angle ratio ($\rho$) affect the throughput, while the grating dimensions S and $g$S impact the manufacturing cost. The form factor $f_{12}$ converts the extremum aberration to the marginal resolution of a scanned line doublet. As for the $f_{21}$ aberration (also of power-sum = 2) discussed in Sec. 4, raytrace scans determined $f_{12} \sim 1/3$ when using an exit slit width which transmits 50% of the diffracted energy at the line peak. The dashed curves in Fig. 3 plot Eq. (49) using $g = 1/4$ and the remaining parameters as previously given. This aberration is seen to be considerably smaller (factors of 10) than the dominant term $(\Delta\lambda_{21}/\lambda)_{\mathrm{sep}}$ for the plane grating.

Use of a curved exit slit to match the shape of this aberration provides additional improvement. As derived in Fig. 5(a), the nominal radius of this slit is fixed by the astigmatism ($\Delta z''_{02}$) and astigmatic curvature ($\Delta x''_{12}$) terms:

$$R_{\mathrm{ex}} = \frac{(\Delta z''_{02}/2)^2}{2\,\Delta x''_{12}} = \frac{({}_{02}z'\cos\psi' + {}_{11}x'\sin\psi')^2\,\sigma^2}{2({}_{12}x'\cos\psi' - {}_{03}z'\sin\psi')\,\sigma^2} = \frac{\eta[(1+1/\eta)+Qc^2\mu/(1+1/\eta)]^2}{[1+(1+Q\tau)c^2]\mu}$$

$$\simeq \left(\frac{2\sin\beta}{c^2\mu}\right)\frac{\eta(1+1/\eta)^2}{(1+1/\rho^2)} \tag{50}$$

where the last expression omits the $\mu$ term in the numerator and is accurate at grazing incidence. The image curvature radius shown in the spot diagram of Fig. 5(b) is r$R_{\mathrm{ex}} \simeq 1615$ mm, with other parameters as follows: $\sin\gamma = 0.052, M = 1, \eta = 2, \rho = 2, \beta = 4^{\mathrm{o}}, \mathrm{L/S} = 12.5, c = 8.664, m = -1, \mu = .0018283, \psi' = -8.607^{\mathrm{o}}$, r = 3m, r′ = 6m.

Optics EXPRESS

Equations (19)-(22) and (34) determine $\Delta z''_{11}/\Delta z''_{02} \approx 2\,\mu\,(\ln 2)\,g^2 q(S/L)\,(\sin\gamma)/\Omega\,/\,(\rho+1)$. If this ratio is less than $1-1/\sqrt{2}$, the slit width ($\Delta x''$) required to include the extremum aberration [Eq. (48)] is less than $\Delta x''_{12}$, as derived from Fig. 5(a):

$$\Delta x''/\Delta x''_{12} = 2[1-(1-\Delta z''_{11}/\Delta z''_{02})^2\,]. \tag{51}$$

In Fig. 5(b), a grating aperture aspect $g = 0.25$, scan range of $q = 3$ octaves and solid angle of $\Omega = 8 \times 10^{-6}$ provide $\Delta z''_{11}/\Delta z''_{02} = 0.0825$, resulting in $\Delta x'' = 0.316\,\Delta x''_{12} = 0.0045$ mm. For marginal line separation, this is multiplied by the form factor of $f_{12}$ to yield a slit width of 0.0015 mm, thereby narrowing the transmitted wavelength profile from $(\Delta\lambda_{12}/\lambda)_{\rm sep} = 2.85 \times 10^{-5}$ (straight slit) to $0.9 \times 10^{-5}$. In the line profile (1D) scan of Fig. 5(c), use of a wider slit (0.003 mm) reveals a net resolution of $\sim 2.5 \times 10^{-5}$, limited by the higher-power term $\Delta\lambda_{31}$ (Sec. 5.3). It is noted that a low value of $g$ not only allows the curved slit to compensate for the increased value of $\Delta\lambda_{12}$ in Eq. (49), but also reduces the $\Delta\lambda_{31}$ aberration in Eq. (53) and provides for a significantly smaller grating. The optimum value for $g$ is set by requiring the ruled width ($gS$) encompass a sufficient number of grooves to achieve the desired diffraction-limited resolution, as determined by Eq. (66).

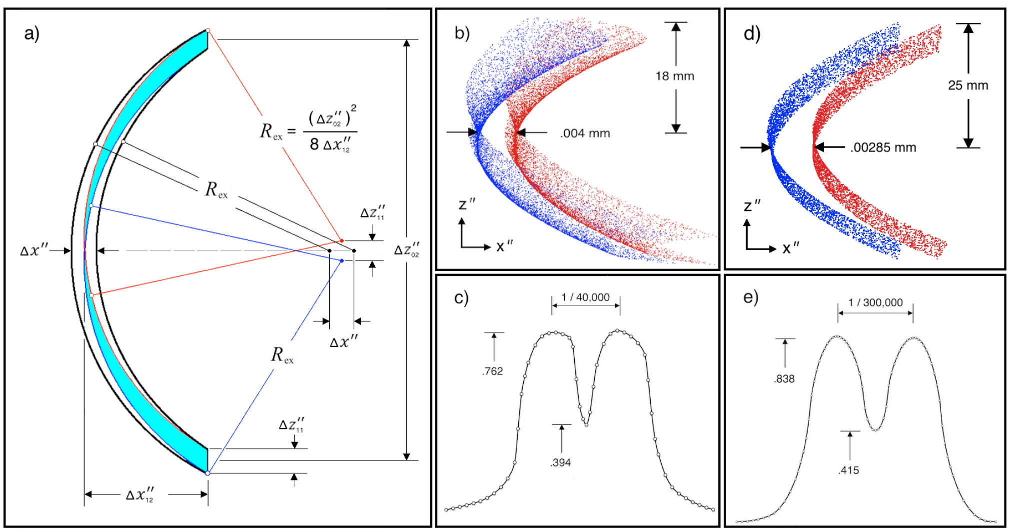


Fig. 5. Numerical raytrace results on the exit plane of a self-focused divergent groove concave grating at a 3° graze angle. The object is a point. (a) Derivation of optimum exit slit curvature and width. (b) Spot diagram for a monochromator length of 9 m, a grating size of 180 mm x 720 mm (may be composed of 4 segments, each 180 mm square), a scan range of 3 octaves, unit magnification, $\rho = 2$, $\phi_{\rm m} \simeq 0.002$ and $\phi_{\rm s} \simeq 0.004$. The "red" and "blue" soft x-ray wavelengths are separated by 1/ 40,000. (c) Spectral scan through a curved exit slit of 0.003 mm width; the 48% dip degrades to the marginal value of 20-25% after adding the physical diffraction width due to the 41,130 grooves illuminated at a maximum scan wavelength of 8 nm. (d) Spot diagram for a monochromator length of 25 m, a grating size of 500 mm x 2000 mm (may be composed of 4 segments, each 500 mm square), a scan range of 1 octave, a "sweet magnification" of 4, $\rho = 1/2$, $\phi_{\rm m} \simeq 0.004$ and $\phi_{\rm s} \simeq 0.002$. The "red" and "blue" soft x-ray wavelengths are separated by 1/300,000. (e) Spectral scan through a 0.002 mm wide curved exit slit; the 50% dip degrades to the marginal value of 20-25% after adding the physical diffraction width due to the 457,000 grooves illuminated at the maximum scan wavelength of 2 nm.

The above choice of unit magnification has the advantages of both minimizing the system length (given a minimum practical slit width) and maintaining the horizontal angular aperture upon diffraction. The resolving power of 40000 shown in Fig. 5(c) compares well with the

Optics EXPRESS

value of 25000 calculated for a recently-proposed single-element plane grating design "SEPGM" [1] otherwise having the same nominal performance ($2\gamma = 6^{\text{o}}$, $\Omega$ = 8 x $10^{-6}$ sr, $\rho = 2$ and $q = 3$). Advantages of the present design are: 1) The mechanically simple and robust scanning motion of rectilinear translation of the grating, contrasting with the multiple correlated rotations of the grating and the slits required with the previous design [1]; 2) At unit magnification ($M = 1$), the system length L = $(1 + M\rho)$r is only ~ 0.64 times that required for the previous design (where $\langle M\rangle = \eta/\langle\rho\rangle$ = 3.7 / 2 = 1.85). This results in a 9 m length, compared to 14.1 m for the SEPGM, given the same object distance (r = 3 m) and exit slit width (0.005 mm would yield a resolving power of ~ 30,000 for the present design and a point object). 3) The potential to maintain peak blaze efficiency at all scanned wavelengths (Sec. 2.2). Disadvantages of the present design are: 1) The need for a meridionally-curved (non-planar) surface; 2) A larger grating (180 mm x 720 mm vs. 214 mm diameter), albeit the long dimension is along the groove lengths and may thus be constructed from an (incoherent) linear array of smaller gratings (e.g. 4 gratings, each 180 mm square); 3) A curved groove pattern; and 4) Restriction to use with a point object, rather than an entrance slit extending out of the meridional plane.

### *5.3 High-power mixed aberration ($\Delta\lambda_{31}$) and a "sweet magnification"*

Equations (30), (31), (32) and (33) determine this 3rd power extremum wavelength aberration. Employing Eq. (42) and neglecting the higher-power terms in Eqs. (30) and (31):

$$\frac{\Delta\lambda_{31}}{\lambda} \simeq 2c\left|3N_{30} + N_{20} - 2 + \left(\frac{3}{2\eta} - \frac{{}_{21}T}{c}\right)\left(\frac{1}{\eta\kappa} - \frac{2}{\eta^2}\right)\right.$$
$$\left. + \left[\eta(Q-1)N_{20} + 1 + Q\left(1 + \frac{{}_{21}T}{c}\right)\right]\right|\frac{c^2\mu}{\eta+1}\,\breve{\varpi}^2\breve{\sigma} \qquad (52)$$

Further simplification uses the previous substitutions for $c$, $Q$, $\breve{\varpi}$ and $\breve{\sigma}$, and the following: ${}_{21}T = ({}_{12}S)\,(\sin\beta)\tan\psi' \simeq c^3\mu/(1+1/\eta) - c$, Eq. (37) for $N_{20}$, Eq. (38) for $N_{30}$, and Eq. (47) for $1/\kappa$, where small-angle approximations are also employed in all terms:

$$\left(\frac{\Delta\lambda_{31}}{\lambda}\right)_{\text{sep}} \simeq \left|{}_{31}F_{\rho,M}\right| g\,\frac{\Omega\, q}{\sin\gamma}\,\frac{\ln 2}{8} f_{31}\,;\ \ {}_{31}\mathrm{F}_{\rho,M} \simeq \left[-\rho^4 + \frac{\rho^2}{M} - \frac{\rho}{M} + \frac{1}{M^2\rho}\right]\frac{6}{(\rho^2-1)(\rho+1)} +$$
$$\left\{\begin{matrix} \frac{7}{2}M\rho^5 + \left(3M + \frac{1}{4}\right)\rho^4 - \left(\frac{9}{2}M + 1\right)\rho^3 - \left(4M - \frac{3}{4}\right)\rho^2 \\ + \left(\frac{1}{2}M + 3\right)\rho + \left(M - \frac{5}{4}\right) + \left(\frac{1}{2}M - 2\right)/\rho + 1/\rho^2\,/4 \end{matrix}\right\}\frac{\mathrm{c}^2\,\mu}{(M\rho+1)(\rho^2-1)(\rho+1)} \qquad (53)$$

and where raytracings find $f_{31} \sim 1/5$. Though Eqs. (52) and (53) are only approximations (~ 1% accuracy), the full and exact Fermat expansion term resulting from Eqs. (30)-(31) agrees precisely (~$10^{-13}$ radians) with the raytraced numerical extraction Eqs. (45)-(46) of Sec. 4.2 The dominant bracketed [ ] term in Eq. (53) vanishes if the magnification is chosen to be

$$M_{\text{sweet}} = 1/\rho^2 \qquad (54)$$

corresponding to $\eta = 1/\rho$. Figure 3 plots two examples: $M_{\text{sweet}} =$ 1/4, showing the cancelation of $\Delta\lambda_{31}$ for an inside spectral order (near $\rho = 2$); and $M_{\text{sweet}} =$ 4, showing the cancelation for an outside spectral order (near $\rho = 1/2$). Figure 5(d) shows the numerical raytrace employing the following parameters: $\sin\gamma = 0.052$, $M = 4$, $\eta = 2$, $\rho = 1/2$, $\beta = 2^{\text{o}}$, L/S = 12.5, $c = 2.888$, $m = +1$, $\mu = .0018283$, $\psi' = +5.762^{\text{o}}$, r = 8.33m and r' =16.67 m. As Eq. (49) reveals that $\Delta\lambda_{12}$ scales with $q^2$, reducing the coverage to 1 octave and use of a curved exit slit of width 0.002 mm encloses the extremum aberration at $\Delta\lambda_{12}/\lambda \sim 2.2 \text{ x } 10^{-6}$. Such a narrow exit slit and long focal length corresponds to an angular uncertainty of only ~ $10^{-7}$ radians. While the rigidity of a preloaded rectilinear-only grating stage maximizes the inherent mechanical stability, residual environmentally-induced changes

Optics EXPRESS

to the angles of incidence and diffraction would likely require optical monitoring and mechanical corrections in real time.

## 6. Aberration correction of a plane grating in non-grazing mounts

### *6.1 Normal incidence reflection or transmission*

Figure 6 illustrates a reflection or transmission grating illuminated at normal incidence. Setting $\alpha = \pi/2$, $\beta = \pi/2 - \beta_*$, $\Gamma = 0$, $\tau = \sin\beta_*$, $\mu = \sin\beta_*$ and $\rho = \cos\beta_*$, where $\beta_*$ is the angle of diffraction relative to the grating normal, Eq. (41) becomes:

$$\frac{\Delta\lambda_{21}}{\lambda} = \left|\left[\frac{\eta + \cos^2\beta_*}{\eta + 1}\right]/\sin\beta_* + \left[\frac{2-\eta^2}{(\eta+1)^2} - \tan^2\psi'\right]\sin\beta_*\right| \left(\frac{\ln 2}{2}\right)\left(\frac{\mathrm{L}}{\mathrm{S}}\right)\left(\frac{\Omega q}{\eta}\right) \qquad (55)$$

in which $\tan\psi' = \mu c/(1 + 1/\eta)/\cos\beta_* = q\eta/(\eta+1)^2(\mathrm{L/S})(\ln 2)\tan\beta_*$. Furthermore, $\eta = M\cos\beta_*$, where $M$ is the horizontal magnification, thus the term in brackets $|\,|$ becomes a quartic in $\cos\beta_*$ whose root yields the condition whereby $\Delta\lambda_{21}/\lambda$ vanishes for any given value of $M$. For example, consider a small grating (S = 32 mm), a short path length from object to image (L = 90 mm) and a scan over the visible spectrum (400-700 nm, thus $q = \log_2(7/4) \approx 0.807$). Numerical iteration of the quartic at a magnification of unity yields the aberration-removal solution of $\cos\beta_* = 0.08367$ ($\beta_* = 85.2^\circ$ and $\eta = 0.08367$); at a magnification of 1.42 it yields $\cos\beta_* = 0.256$ ($\beta_* = 75.2^\circ$ and $\eta = 0.369$); and at a magnification of 2 yields $cos\beta_* = 0.344$ ($\beta_* = 69.9^\circ$ and $\eta = 0.688$).

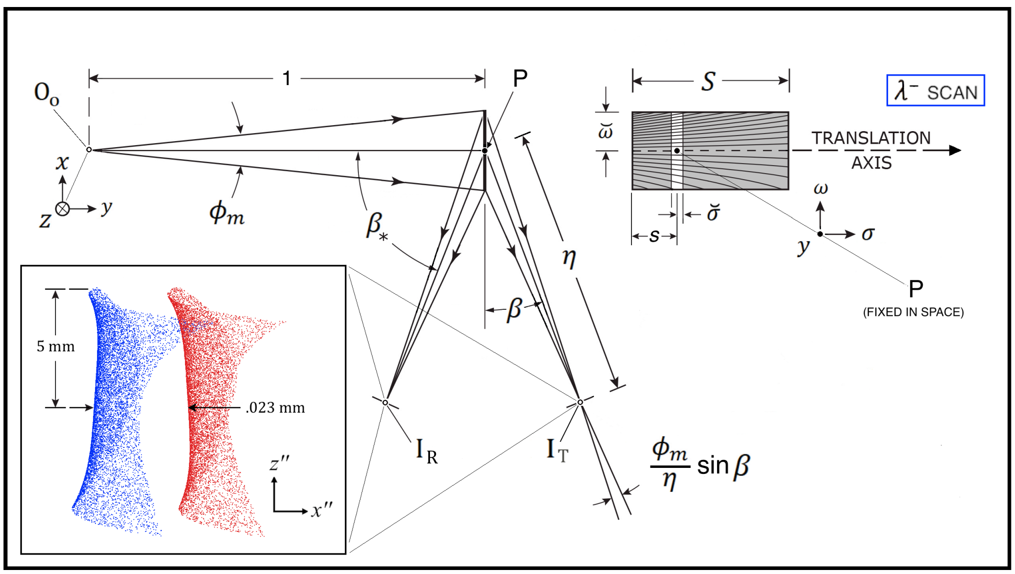


Fig. 6. Normal incidence mount of a self-focused divergent groove grating, with the diffracted beam either transmitted ($I_T$) or reflected ($I_R$). The parameters raytraced are $\overline{\mathrm{O_oP}} = 53$ mm, $\overline{\mathrm{PI}} = 37$mm, $\beta = 20.1^\circ$, $M = 2$, $\phi_\mathrm{m} = .20$, $\phi_\mathrm{s} = .0125$, $2\breve{\omega}\mathrm{r} = 10.75$ mm, $2\breve{\sigma}\mathrm{r} = 0.66$ mm and a spectral scan from 400 nm to 700 nm over a translation of $S\mathrm{r} = 32$ mm. The spot diagram is a numerical raytracing at 2 wavelengths (colored here in red and blue) separated by twice the marginal resolution of 1/6000, with the images being identical in transmission and reflection. An exit slit would be aligned to the $z''$-axis (image length direction) which makes the fixed angle $\psi' = 46.0642^\circ$ relative to the $z$-axis shown in the optical schematic.

The other mixed term of power-sum $= 2$ is sagittal coma, obtained from Eq. (48):

$$\frac{\Delta\lambda_{12}}{\lambda} = \left|\left[1 + (1 + \tan^2\beta_*)\, q^2 \left(\frac{\mathrm{L}}{\mathrm{S}}\right)^2 \frac{(\ln 2)^2}{(\eta+1)^2}\right]\right| \frac{{\phi_\mathrm{s}}^2}{8} \qquad (56)$$

yielding $\Delta\lambda_{12}/\lambda \approx 0.0026$ for a square aperture of $\phi_m = \phi_s = 0.05$. However, the aberration is reduced by a factor of 16 (at the same solid aperture) by increasing $\phi_m$ to 0.20 and reducing $\phi_s$ to 0.0125. The resulting $\Delta\lambda_{12}/\lambda = 0.000163$ is verified by $\mathrm{r}\,\Delta x''_{12} = 0.011$ mm extracted from the (independent) raytrace spot diagram inset to Fig. 6, and use of Eq. (33). Also extracted is $\mathrm{r}\,\Delta x''_{31} = 0.025$ mm, in agreement with Eqs. (30)-(32). Multiplying these extrema values by $f_{12} = 1/3$ and $f_{31} = 1/5$ yields the marginal aberrations. The net resolution then includes the contributions from Eq. (65) for dispersion (assuming 0.004 mm widths for both the object and the exit slit) and Eq. (66) for physical diffraction from 14400 grooves (at the low-density end of 1341 g/mm), yielding $(\Delta\lambda/\lambda)_{\mathrm{sep}} \approx 1/6000$.

### *6.2 Littrow (retroreflection)*

A self-focusing plane reflection grating mounted in or near Littrow (Fig. 7) and capable of wavelength scanning on-blaze provides an efficient and compact monochromator for the UV, visible or near IR regions. Setting $\alpha = \pi - \beta$, $\Gamma = -1$, $\mu = 2\sin\beta_*$ and $\rho = 1$ in Eq. (41):

$$\frac{\Delta\lambda_{21}}{\lambda} = \left|\frac{1}{2} + \left[\frac{2}{(\eta+1)^2} - \tan^2\psi'\right]\tan^2\beta_*\right|\left(\frac{\ln 2}{2}\right)\left(\frac{\mathrm{L}}{\mathrm{S}}\right)\left(\frac{q}{\eta}\right)\frac{\phi_m\,\phi_s}{\tan\beta_*} \tag{57}$$

in which $\tan\psi' = q\eta/(\eta+1)^2(\mathrm{L/S})(2\ln 2)\tan\beta_*$. The term in brackets $|\,|$ is thereby a quadratic in $\beta_*$ whose root yields the condition whereby this aberration vanishes. To horizontally retro-focus the object (at a magnification of $-1$), one chooses $\eta = 1$. To facilitate construction of a monochromator, the object (or entrance slit) and image (or exit slit) may be displaced in $x$ (a "near-Littrow" configuration). In a very compact configuration, $\mathrm{L} = 90$ mm ($\mathrm{r}' = \mathrm{r} = 45$ mm), $\Omega = \phi_m\,\phi_s = 0.0025$ and $q = 0.807$, the above solution for $\Delta\lambda_{21}/\lambda = 0$ is $\beta_* = 49.696^{\circ}$.

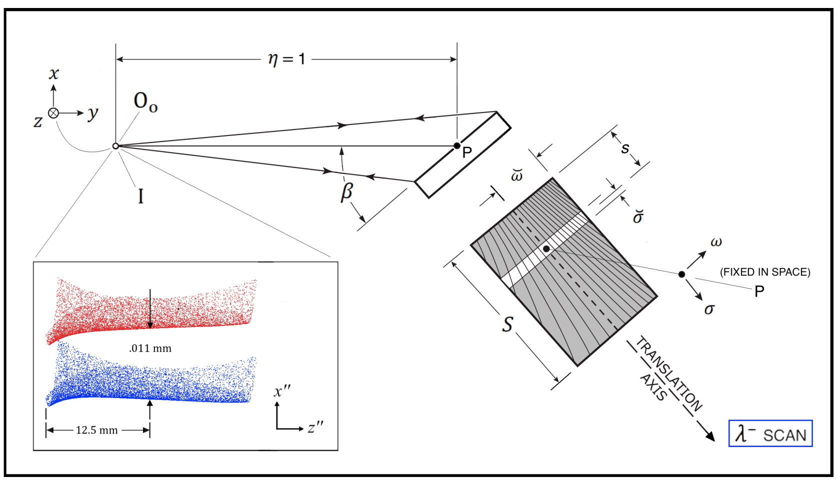


Fig. 7. Littrow mount of a divergent groove grating in a retro-focus configuration. The parameters raytraced are $\overline{\mathrm{O_oP}} = \overline{\mathrm{P\,I}} = 45$ mm, $\beta = 40.3^{\circ}$, $M = -1$, $\phi_m = 0.200$ and $\phi_s = 0.0125$, $2\breve{\omega}\mathrm{r} = 14.3$ mm, $2\breve{\sigma}\mathrm{r} = 0.562$ mm and a spectral scan from 400 nm to 700 nm over a translation of $S\mathrm{r} = 32$ mm. The spot diagram is a numerical raytracing at two wavelengths (colored here in red and blue) separated by twice the marginal resolution of 1/14000. An exit slit would be aligned to the $z''$-axis (image length direction) which makes the fixed angle $\psi' = 42.8432^{\circ}$ relative to the $z$-axis shown in the optical schematic.

The remaining aberration is dominated by Eq. (27):

$$\frac{\Delta\lambda_{12}}{\lambda} = \left|\left[1 + (1 + 2\tan^2\beta_*)\,q^2\left(\frac{\mathrm{L}}{\mathrm{S}}\right)^2\frac{(\ln 2)^2}{(\eta+1)^2}\right]\right|\frac{{\phi_s}^2}{8}. \tag{58}$$

Given $\phi_{\rm s} = 0.0125$ and $\phi_{\rm m} = 0.200$, Eq. (58) provides $\Delta\lambda_{12}/\lambda = 0.000065$, verified by r $\Delta x''_{12} = 0.005$ mm extracted from the raytrace inset to Fig. 7. Also extracted is r $\Delta x''_{31} =$ 0.008 mm, in agreement with Eqs. (30)-(32). Multiplying these extrema values by $f_{12} = 1/3$ and $f_{31} = 1/5$ yields the marginal aberrations. The net resolution then includes the contributions from Eq. (65) for dispersion (assuming 0.004 mm widths for both the object and the exit slit) and Eq. (66) for physical diffraction from 31000 grooves (at the low-density end of 2179 g/mm), yielding $(\Delta\lambda/\lambda)_{\rm sep} \approx 1/14000$. It is noteworthy that this ultra-high resolution single-element scanning system is only 45 mm in length. Given the object distance is r = L/$(1+\eta)$ and the image distance is r' = L/$(1+1/\eta)$, the monochromator length along its y-axis in Figs. 6 and 7 is between L and L/2, depending upon $\eta$ and $\beta$.

Equations (55)-(58) have been verified by extractions of these power terms from numerical raytracings. Similar resolution may be obtained for other high angular deviation plane grating mountings (e.g. for “near-normal” monochromators). This is due to the ability to balance the component terms of $\Delta\lambda_{21}$ in different powers of $\mu$ [e.g. see Eq. (55)], where $\mu = \sin\beta_*$. However, such balancing is not possible at a low angular deviation $2\gamma$ (grazing incidence) where $\mu \ll 1$ per Eq. (9). Due to the very high meridional aperture (0.20 radians), the spot diagrams in Figs. 6 and 7 contain a small amount (0.002 mm) of r $\Delta x''_{60}$. This high-power S-shaped aberration may be easily corrected by a nonzero value of $N_{60}$, though not accomodated in the current raytrace routine. However, a nonzero value of $N_{50}$ was used to remove the high-power r $\Delta x''_{50}$ term, which would have otherwise added a U-shaped aberration of magnitude 0.002 mm in Fig. 6 and 0.006 mm in Fig. 7.

## 7. Inclusion of an entrance slit

### 7.1 Tilt angle and curvature: principal ray terms

In Eqs. (35) and (36), the tilt angle $\psi'$ of the exit slit was determined by the paraxial focusing of sagittal and meridional rays originating from a single object point in the horizontal (meridional) plane. In Fig. 2, this “in-plane” point is designated $\rm O_o$ and defines the origin (0,0). Now consider an infinitesimal width entrance slit centered on this point, but extending a finite distance $(z)$ out of the horizontal plane. To avoid image broadening due solely to the off-plane position $(x, z)$ of a self-luminous object point (O) along this slit, the (principal) ray $\overrightarrow{\rm OP}$ from this point to the grating pole must be reflected to an image point $_{\rm p}$I which also lies along the in-plane image orientation given above. Figure 2 illustrates a general object point (open circle) and its principal ray (dashed). The algebraic solution constrains not only the entrance slit tilt angle ($\psi$), but also its curvature radius ($R_{\rm en}$) and higher derivatives of a polynomial function specifying the horizontal coordinate $x = \sum z^k\,(1/k!)\,\partial^k x/\partial z^k$, where $\partial x/\partial z = \tan\psi$ and $\partial^2 x/\partial z^2 = 1/R_{\rm en}$. Using the general equation of a recent paper [1, Eq. (11)] and substituting $\theta = 0$ for the present grating mount:

$$\tan\psi = -\rho\tan\psi' = -\frac{\rho\,\mu\,c}{(1+1/\eta)\sin\beta} \simeq \frac{(\rho-1)}{(1+1/\eta)}\,c\sin\gamma \tag{59}$$

$$R_{\rm en} = -\left[\frac{(\sin\beta)\cos\psi}{\rho\,\mu}\right] \Big/ \left[1+\frac{(1-\Gamma\rho^2)}{(1+1/\eta)^2}\tau Q c^2\right] \simeq \frac{2\cos\psi}{c^2\sin\gamma}\left[\frac{(1+1/\eta)/\eta}{\rho\,(1+\rho)(1-1/\rho)^3}\right]. \tag{60}$$

The coefficient of the next higher degree $(\partial^3 x/\partial z^3)$ was obtained by numerical optimization. As the independent variables ($\psi', \rho, c$ and $\gamma$) are fixed, the entrance slit tilt angle and its shape coefficients are also fixed. For example, given the parameters used for the Fig. 4 raytrace ($\gamma = 3^{\rm o}$, $\rho = 2$, $\eta = 2$, and r = 166.67 mm), the above equations determine $\tan\psi = -2\tan\psi' =$ 0.3027 and $R_{\rm en} =$ 78.9 mm, confirmed by the numerical raytracing shown in Fig. 8. This curvature corresponds to a deviation of 0.16 mm at the ends of a 10 mm long slit. Such a correction is of practical advantage only if it is larger than the grating

Optics EXPRESS

aberrations, including those resulting from object points along this tilted slit. It is also noted that, instead of curving the entrance slit by $R_{en}$, the exit slit could be curved to a radius of $R_{ex} = \eta\rho R_{en}/\cos\psi$, equal to 329.7 mm using the above parameters. However, Fig. 8 shows this induces significantly larger off-axis spectral aberrations.

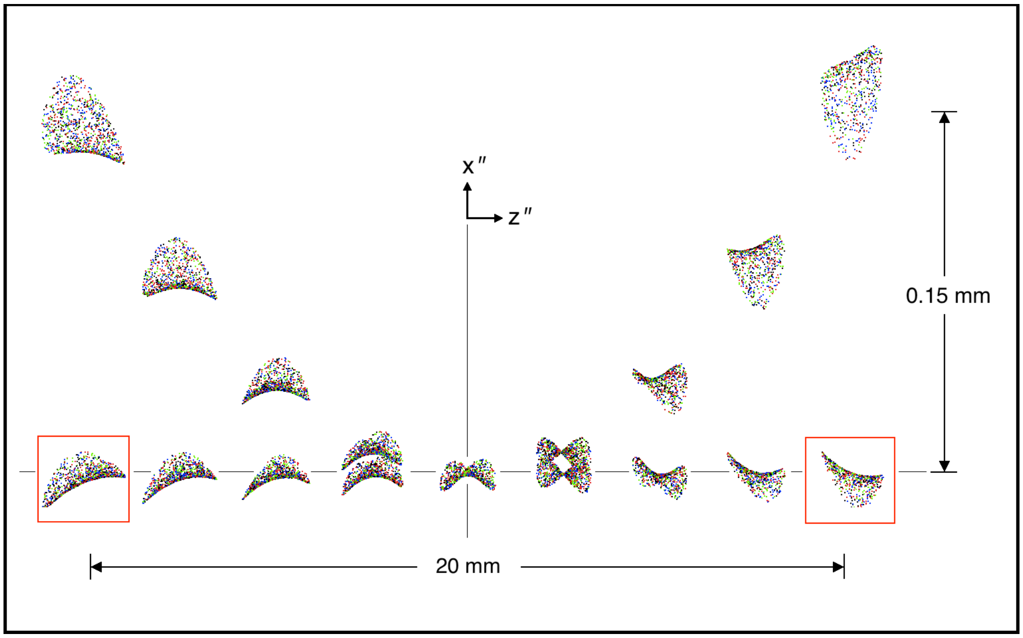


Fig. 8. Raytraced spot diagrams. The plane grating image at the origin is the same as given in Fig. 4(a), while the other 16 are for off-plane object points. These are spaced at 1.25 mm intervals along a 10 mm long entrance slit, which is tilted by $+16.84°$ in accordance with Eq. (59). The upper sequence of images (whose centers lie along a parabolic curve) result from a straight entrance slit; the lower sequence of images (whose centers lie on the $z''$ axis) result from an optimally-curved entrance slit [e.g. the radius given by Eq. (60)]. The individual aberration terms extracted from the two spot diagrams at the extreme edges (outlined in red) are: $\Delta x''_{111}(\text{tilt}) = 0.0175$ mm, in agreement with Eq. (62); $\Delta x''_{201}(\text{defocus}) = 0.0030$ mm, in agreement with Eq. (63); $\Delta x''_{301}$ (coma) $= 0.0029$ mm and $\Delta x''_{401}$ (spherical aberration) $=$ 0.00026 mm. These combine to yield a net broadening of $\Delta x''_{net} \sim 0.005$ mm, added to that of the on-axis image. Note that the magnification from object to image is unity in the spectral direction ($x''$), but is $\simeq \eta = r'/r = 2$ in the slit length direction ($z''$).

### *7.2 Off-axis grating spectral aberrations*

The object points along a finite length entrance slit deviate from the on-axis (0,0) point in both the vertical and horizontal directions. This induces additional wavelength aberrations:

$$\Delta\lambda_{ijh}/\lambda = p_{ij}\left|_{ijk}\Delta\lambda/\lambda\right|(2\breve{\omega})^{i-1}(2\breve{\sigma})^{j}\, z^{k}. \tag{61}$$

These terms arise mainly from the slit tilt of Eq. (59), which results in a nonzero horizontal coordinate $x = z\tan\psi$. This changes the meridional angle incident to the grating and thus the image tilt ($i = 1, j = 1$), the focal length ($i = 2$ and $j = 0$) and higher-power terms (not derived here by expansion of the light-path, but quantified by extraction from numerical raytracings). For a plane grating, the dominant term in Eq. (61) is image tilt, having a total power-sum $\equiv\ i + j - 1 + k = 2$. Expansion of the light-path (Sec. 3.1) yields:

$$_{111}\Delta\lambda/\lambda = (1 + 1/\eta)\,(\tan^2\psi')\,\tau/\mu + 1 \simeq (1 + 1/\eta)\,(\tan^2\psi')/\mu + 1 \tag{62}$$

which is valid for both the plane and meridional-only curved (cylindrical) gratings.

Optics EXPRESS

The other lateral aberration of power-sum = 2 is the defocus term, whose expansion coefficient for a plane grating (e.g. as employed in Sec. 4) is:

$$\begin{aligned} {}_{201}\Delta\lambda_{\text{plane}}/\lambda &= [(1+1/\eta)\tan^2\psi' + (\Gamma - 1)]\tau\,(\tan\psi')\,(\sin\beta)/\mu \\ &\simeq [(1+1/\eta)\,(\tan^2\psi')/\mu - 1](\tan\psi')\sin\beta. \end{aligned} \tag{63}$$

If $\breve{\sigma}/\breve{\omega} \sim \sin\beta$ (giving equal horizontal and vertical angular apertures in the diffracted beam), $\Delta\lambda_{201}/\Delta\lambda_{111} \sim \tan\psi'$ for a plane grating. However, for the concave grating (Sec. 5), Fermat expansion and raytracing reveals a substantial increase in the defocusing term:

$$\begin{aligned} \frac{{}_{201}\Delta\lambda_{\text{curved}} - {}_{201}\Delta\lambda_{\text{plane}}}{\lambda} &= 2\tau\frac{\Gamma\rho + 1}{(\rho+1)^2}\left(\rho^2 + \frac{1}{\eta}\right)\frac{\tan\psi'}{\mu}\sin\beta \\ &\simeq 2\left(\frac{\rho^2 + 1/\eta}{\rho + 1}\right)\frac{\tan\psi'}{\mu}\sin\beta. \end{aligned} \tag{64}$$

This is due to the tilt of the entrance slit, which changes the meridional graze angle and thus the focal length of the grating. From Eqs. (61) and (64), the maximum length entrance slit which may be used while preserving the resolution of 1/40000 for the unit magnification concave grating monochromator (Sec. 5) is only $2\breve{z}$r = 0.072 mm. This restricts the ultra-high resolution, concave divergent groove monochromator to use with a pointlike object.

## 8. Physical considerations

### *8.1 Linear dispersion*

Differentiation of Eq. (9) yields the contribution to the fractional FWHM spectral resolution from an exit slit of effective width $\Delta x''_{\text{eff}} \approx \text{MAX}(\Delta x'', M\Delta x) + \frac{1}{2}\text{MIN}(\Delta x'', M\Delta x)$:

$$(\Delta\lambda/\lambda)_{\text{dispersion}} = \frac{\Delta\beta\,\sin\beta}{\cos\beta - \cos\alpha} \simeq \left(\frac{\Delta x''_{\text{eff}}}{M\cos\psi'}\right)\frac{D}{\text{L}} \tag{65}$$

where $D = (1+1/\eta)/\tan\beta_*$ at normal incidence $(\alpha = \pi/2)$, $D = (1+1/\eta)/(2\tan\beta_*)$ at Littrow $(\alpha = \pi - \beta)$ and $D \simeq |(M\rho + 1)/(\rho - 1)|/\sin\gamma$ at grazing incidence $(\gamma \ll 1)$. At grazing incidence, the $1/|\rho - 1|$ dependence encourages a larger value of $\rho$ (or $1/\rho$ in the case of an outside spectral order), apart from any additional advantage this provides in decreasing the contribution from geometrical aberrations (see Fig. 3). The unit magnification design of Sec. 5.2 ($\rho = 2$ and $\gamma = 3^{\text{o}}$) requires $\Delta x''_{\text{eff}} = 0.003$ mm ($\Delta x'' = 0.003$ mm, $\Delta x = 0$) to provide $(\Delta\lambda/\lambda)_{\text{dispersion}} \sim 2.0 \times 10^{-5}$ for a monochromator length of L = 9 m. For the most compact (L = 0.5 m) plane grating design proposed in Sec. 4.2, entrance and exit slits each of width 0.004 mm yield $(\Delta\lambda/\lambda)_{\text{dispersion}} = 0.7 \times 10^{-3}$.

### *8.2 Diffraction limit*

As the concave grating monochromator (Sec. 5) cancels nearly all spectral aberrations, the contribution from physical diffraction is non-negligible. The Rayleigh criterion specifies:

$$(\Delta\lambda/\lambda)_{\text{diffraction}} = \frac{1}{|m|N} \simeq \frac{\text{d}\sin\alpha}{m\,\text{r}\,\phi_{\text{m}}} \simeq \left(\frac{\lambda}{\phi_{\text{m}}}\right)\frac{D}{\text{L}}. \tag{66}$$

Comparison with Eq. (65) reveals that $(\Delta\lambda/\lambda)_{\text{diffraction}}/(\Delta\lambda/\lambda)_{\text{dispersion}} = (\lambda/\Delta x''_{\text{eff}})/(M\phi_{\text{m}})$. Given $M = 1$ and $\phi_{\text{m}} \simeq 0.002$, this ratio is unity at the longest scan wavelength ($\lambda = 8$ nm) for $\Delta x''_{\text{eff}} = \Delta x'' = 0.004$ mm. At $\gamma = 3^{\text{o}}$ and $\rho = 2$, Eq. (66) yields $(\Delta\lambda/\lambda)_{\text{diffraction}} = 2.5 \times 10^{-5}$ for the large (L = 9 m) concave grating monochromator of Sec. 5.2 (ruled width = 180 mm). For the most compact plane grating monochromator of Sec. 4.2, $(\Delta\lambda/\lambda)_{\text{diffraction}} = 4.5 \times 10^{-4}$ (ruled width = 13.5 mm).

Finally, consider the very large (L = 25 m, ruled width = 500 mm) nearly aberration-free monochomator proposed in Sec. 5.3. With $M = 4, \rho = 0.5$ and $\phi_{\mathrm{m}} = 0.004$, Eq. (66) yields $(\Delta\lambda/\lambda)_{\mathrm{diffraction}} \simeq 2.2 \times 10^{-6}$ at 2 nm ($q = 1$), equal to the contribution from Eq. (65) due to a 0.002 mm wide exit slit. The sum of these two effects thereby yields the resolution of $(\Delta\lambda/\lambda)_{\mathrm{sep}} \simeq 3.3 \times 10^{-6}$ shown in Fig. 5(e).

## 9. Conclusions

A new geometry has been proposed, whereby simple translation of a curved groove pattern along its central straight groove provides wavelength scanning within a fixed optical geometry. As a first result, a single-element monochromator employing a self-focusing such grating has been introduced and its imaging performance analyzed in detail. The spectral aberrations in pure meridional powers of the grating aperture were shown to vanish at all scanned wavelengths, at all angles of incidence (normal to grazing) and in either transmission or reflection. Additionally, the following parameters were also constrained to be independent of the scanned wavelength: the residual aberration, the image and object tilt angles, the beam aperture and (with advanced etching of the groove profiles) the relative diffraction efficiency.

A table-top ($0.5 - 1$ m in length) grazing incidence plane grating configuration of this monochromator scans 3 octaves in the soft x-ray (e.g. $\lambda = 1 - 8$ nm) at unit magnification, a resolving power of 1000-2000 and a collection angle of $8 \times 10^{-6}$ sr. Without degrading the resolution, the throughput of spatially extended sources may be significantly increased by use of a long entrance slit (fixed curvature) while maintaining a straight exit slit. A large (9 m) version employs a concave grating surface to eliminate the dominant geometrical aberration, providing $\lambda/\Delta\lambda \sim 4 \times 10^{4}$, but is restricted to use with a pointlike object. At a "sweet magnification" of 4, the scanned spectrum is nearly free of geometrical aberrations, enabling diffraction-limited resolutions of $\lambda/\Delta\lambda \sim 3 \times 10^{5}$ over one octave in wavelength. This ultimate design comprises $> 10^{5}$ spectral bins per grating, however the requirements on exit slit width (0.002 mm) and system length (25 m) raise issues of stability. At normal incidence (transmission or reflection) or in Littrow (retro-reflection), the dominant plane grating aberration may be removed by judicious choice of the diffracted angle. This enables high spectral resolution ($\lambda/\Delta\lambda \sim 10^{4}$) while maintaining the practical advantage of a plane surface for miniature-sized monochromators for applications in the UV to the infrared.

The above gratings may be written by existing maskless lithography systems using visible or UV lasers at exposed feature sizes of ~ 500 nm to 200 nm (1/d $\lesssim$ 2500 g/mm), with a low integrated level ($10^{-3}$) of stray light expected for 1/d $\lesssim$ 250 g/mm. For higher densities, the groove placement accuracy should be improved by upgrading the environmental and interferometer control sub-systems in these commercial pattern writers to those used for mechanical ruling engines. For plane gratings, commercial DUV projection lithography can reduce a transmissive mask made by the above process, providing a (smaller) grating having 4 times the groove density (1/d $\lesssim$ 10000 g/mm) at the same stray light level as the master.

The proposed new method of scanning wavelength is not restricted to a particular focusing condition or geometry. Though this introductory paper has presented in detail the example of a single-element astigmatic in-plane grating mount, several other applications of this method are under study. These include adding wavelength tunability to prior fixed-grating spectrograph geometries, multi-element (e.g. stigmatic and common path-length) systems and an extreme off-plane grating mount, where the central groove is oriented meridionally.

## Acknowledgment

The author thanks Dr. Michael Lampton for upgrading his open-source numerical raytrace code (BEAM4) to include two-dimensional VLS density coefficients ($V_{ij}$), as required for the curved groove grating introduced in this paper. For some years, BEAM4 has been an invaluable "gold standard" to confirm the accuracy of this author's light-path formulations.